TÜBİTAK

Turkish Journal of Earth Sciences

http://journals.tubitak.gov.tr/earth/

Research Article

Turkish J Earth Sci
(2019) 28: 410-437

doi:10.3906/yer-1810-6

Holocene seismic activity of the Priene–Sazlı Fault revealed by cosmogenic ^{36}Cl, Western Anatolia, Turkey

Nasim MOZAFARI[1,*], Ökmen SÜMER[2], Dmitry TIKHOMIROV[1,3], Susan IVY-OCHS[4], Vasily ALFIMOV[4], Christof VOCKENHUBER[4], Uğur İNCİ[2], Hasan SÖZBİLİR[2], Naki AKÇAR[1]

[1]Institute of Geology, University of Bern, Bern, Switzerland
[2]Department of Geological Engineering, Faculty of Engineering, Dokuz Eylül University, İzmir, Turkey
[3]Geographical Institute, University of Zürich, Zürich, Switzerland
[4]Laboratory for Ion Beam Physics, Swiss Federal Institute of Technology (ETH), Zurich, Switzerland

Received: 17.10.2018 • **Accepted/Published Online:** 04.03.2019 • **Final Version:** 10.05.2019

Abstract: Fault scarps in carbonates are structures well suited to ^{36}Cl analysis of paleoearthquakes to reconstruct the seismic history using cosmogenic ^{36}Cl. In this study, we measured cosmogenic ^{36}Cl concentrations in 117 samples along one of the active faults in Western Anatolia, the Priene–Sazlı Fault scarp, to reconstruct the age of paleoearthquakes along with their slip amounts, beyond the available historical and instrumental archives. Our results indicate four periods of high seismic activity on the Priene–Sazlı Fault since the early Holocene at 8.1 ± 2.0, 6.0 ± 1.5, 3.7 ± 0.9, and 2.2 ± 0.5 ka, with slips of 3.4 ± 0.5, 1.5 ± 0.2, 1.4 ± 0.2, and 1.5 ± 0.2 m, respectively. These ruptures mostly occurred as clusters of earthquakes with magnitudes of up to 6.7–7.0 during the Holocene. Estimated slip rates on the fault are greater than 0.3, 0.7, 0.6, and 1.0 mm/year from the oldest to the youngest modeled earthquakes. In addition, the long-term slip rate is 0.7 mm/year. This means that the Priene–Sazlı fault can be considered as a low to moderately seismogenic fault, based upon the recurrence interval.

Key words: Fault scarp, ^{36}Cl dating, Western Anatolia, active fault, horst-graben

1. Introduction

The displacement history of faults, along with the magnitude of their associated destructive earthquakes, provides essential data to assess the recurrence interval of earthquakes and to estimate the likelihood of their occurrence in the future (e.g., McCalpin, 2009). Generally, major earthquakes produced by faults have recurrence intervals of several hundred years (e.g., Molnar, 1979; Scholz, 2002). This has been demonstrated in the historical and instrumental earthquake records from around the world: e.g., Turkey (Ambraseys, 1971), Greece (Pantosti et al., 1996; Pavlides, 1996; Caputo et al., 1998), and northeastern China (Lee et al., 1976). The oldest known historical records of earthquakes report earthquakes in eastern Crete and Sodom (Judaea, in the vicinity of the Dead Sea) in the Eastern Mediterranean region, which occurred between 2100 and 1700 BCE (Shebalin et al., 1974; Soysal et al., 1981; Ambraseys, 2009). However, instrumental recording of destructive earthquakes only began at the end of the 19th century.

The time span covered by the historical and instrumental archives is too short for the full reconstruction of earthquake recurrence intervals on the order of thousands of years. Nevertheless, the analysis of the long-term seismic behavior of faults with recurrence intervals of >1000 years based on the existing records can wrongly imply inactivity of the respective fault. Misestimation of such fault behavior can cause extensive devastation of urban areas and their infrastructure and the loss of many thousands of lives. Therefore, accurate seismic data that predate the existing written archives are vital in assessing the vulnerability of settlements and designing systems to mitigate the effects of earthquakes.

Seismic data that precede instrumental and historical data are generally tracked by paleoseismological trenching, which is the most common method applied to determine the displacements of faults and recurrence intervals of earthquakes (e.g., McCalpin, 2009). In this technique, the amount of displacement is determined according to the offset of clear piercing points, such as soil horizons, folds, fissures, and channel structures. The timing of the earthquakes is then indirectly dated, mostly by ^{14}C and/or optically stimulated luminescence methods, depending on the type of materials contained in the sampling horizons.

* Correspondence: nasim.mozafari@geo.unibe.ch

The best direct evidence for past earthquakes is bedrock fault scarps since they are the only remaining indication of seismic activity. The pace of seismic ruptures on a fault plane can be traced by terrestrial cosmogenic nuclides produced in situ; hence, episodes of dormancy and activity can directly be deciphered (e.g., Cowie et al., 2017). So far, ^{36}Cl seems to be the only suitable cosmogenic nuclide for use in the analysis of past ruptures, although other nuclides, such as cosmogenic ^{10}Be, have been tested in a few studies (e.g., Kong et al., 2010).

Western Turkey is subject to intensive seismic activity and has records of many destructive earthquakes in history (Figures 1 and 2). High seismic activity and consequent normal faulting in carbonate bedrock make this region an ideal natural laboratory to investigate periods of seismic activity beyond the historical and instrumental data. It is essentially characterized by well-exposed limestone scarps beside Quaternary sedimentary basins (Figures 1 and 3) (e.g., Gürer et al., 2001; Sümer et al., 2013).

With this focus, we investigated the paleoseismic history of the Priene–Sazlı Fault from the early Holocene onwards and determined its seismic behavior. Therefore, our objectives are to: (1) identify past ruptures and reconstruct the chronology of the Priene–Sazlı Fault activity; (2) determine the average slip rates; (3) calculate the recurrence period of destructive earthquakes; and (4) estimate the magnitude of future earthquakes. To achieve these goals, we selected a well-exposed surface on the Priene–Sazlı Fault at the lowermost level of successive scarps. This site is close to the epicenter of the 1955 CE earthquake and the ancient city of Priene. A total of 117 samples along four strips were collected for cosmogenic ^{36}Cl analysis. We used the Fault Scarp Dating Tool (FSDT) (Tikhomirov, 2014), a MATLAB code developed to analyze measured cosmogenic ^{36}Cl concentrations (Appendix C). According to our results and based on the modeled vertical components of slips, the Priene–Sazlı Fault experienced at least four major periods of earthquakes with average magnitude of 6.8 during the Holocene.

2. Western Anatolian Extensional Province

The complex deformation framework of the Mediterranean region is a result of the collision of the African and Eurasian plates in the Alpine–Himalayan belt (e.g., Dewey and Şengör, 1979; Şengör and Yılmaz, 1981; Jackson and McKenzie, 1988). The African plate is subducting beneath the Aegean plate at a rate of up to 40 mm/year, parallel to the Hellenic arc (Shaw and Jackson, 2010). This framework contains one of the most seismically active regions in the world, namely the 300-km-wide Western Anatolian Extensional Province (inset map in Figure 1) (e.g., Dewey and Şengör, 1979; Şengör et al., 1985; Seyitoğlu and Scott, 1991; Taymaz et al., 1991; Pavlides, 1996). Western Anatolia is characterized by roughly E-W trending major graben systems, such as the Büyük Menderes, Küçük Menderes, and Gediz (Figure 1). The initiation of the extensional tectonic regime and its rate is still debated. There are two main points of view regarding the beginning of graben formation: (1) the age of extension is defined to be Upper Miocene (Serravallian-Tortonian) or younger (e.g., Dumont et al., 1979; Şengör, 1979; Angelier et al., 1981; Yılmaz et al., 2000; Gürer et al., 2009); and (2) some grabens such as the Büyük Menderes and Gediz are older structures formed since the end of the Oligocene-Lower Miocene (e.g., Seyitoğlu and Scott, 1992; Seyitoğlu et al., 1992, Emre and Sözbilir, 1997; Sözbilir, 2005). The rate of extension is also controversial and ranges from 6 to 30 mm/year (Eyidoğan, 1988; Aktug et al., 2009; Oner and Dilek, 2011).

2.1. The Büyük Menderes Graben and Priene–Sazlı Fault

The Büyük Menderes Graben (BMG) is a roughly arc-shaped structure, 140 km long and 2–14 km wide (e.g., Seyitoğlu and Scott, 1992; Bozkurt ,2000; Çiftçi and Bozkurt, 2009; Gürer et al., 2009). The graben system extends from the Denizli Basin in the east (E-W trending) to the Aegean Sea in the west (NE-SW) (Figure 1). The Menderes Massif borders the BMG to the north and south. The gentle topography of the southern part of the graben, in comparison to the northern side, gives rise to its asymmetric morphology (Gürer et al., 2009). Furthermore, the central part of the graben is lower than both the western and eastern parts. The Büyük Menderes Fault Zone is the northern border of the BMG horst-graben structure, with faulting extending along the entire length of its northern edge (Figure 1). The fault zone is composed of six main segments, each with individual morphological and geological characteristics. These segments form an en-echelon structure, in which the lengths and geomorphological heights of the segments increase from 7 to 40 km and from 1 to 200 m, respectively, from east to west (Altunel et al., 2009; Emre et al., 2016). Along the active Büyük Menderes Fault Zone, well-exposed archeological sites (e.g., Priene) have been discovered, where destructive earthquakes caused damage during both the historical period and the 20th century (Figure 3) (Altunel, 1998; Yönlü et al., 2010).

The Priene–Sazlı Fault is located at the westernmost end of the Büyük Menderes Graben (Figures 1 and 3). The fault is the longest in the entire Büyük Menderes Fault Zone and extends along the margin of Samsun Mountain (Figure 3). Altunel et al. (2009) considered the Priene–Sazlı Fault to be 30 km long, whereas Sümer et al. (2013) asserted that the total fault length is 37 km (including the 30-km Priene segment and a section of the Sazlıköy segment of Altunel et al., 2009), based on the similarity of the geometry and kinematics. According to

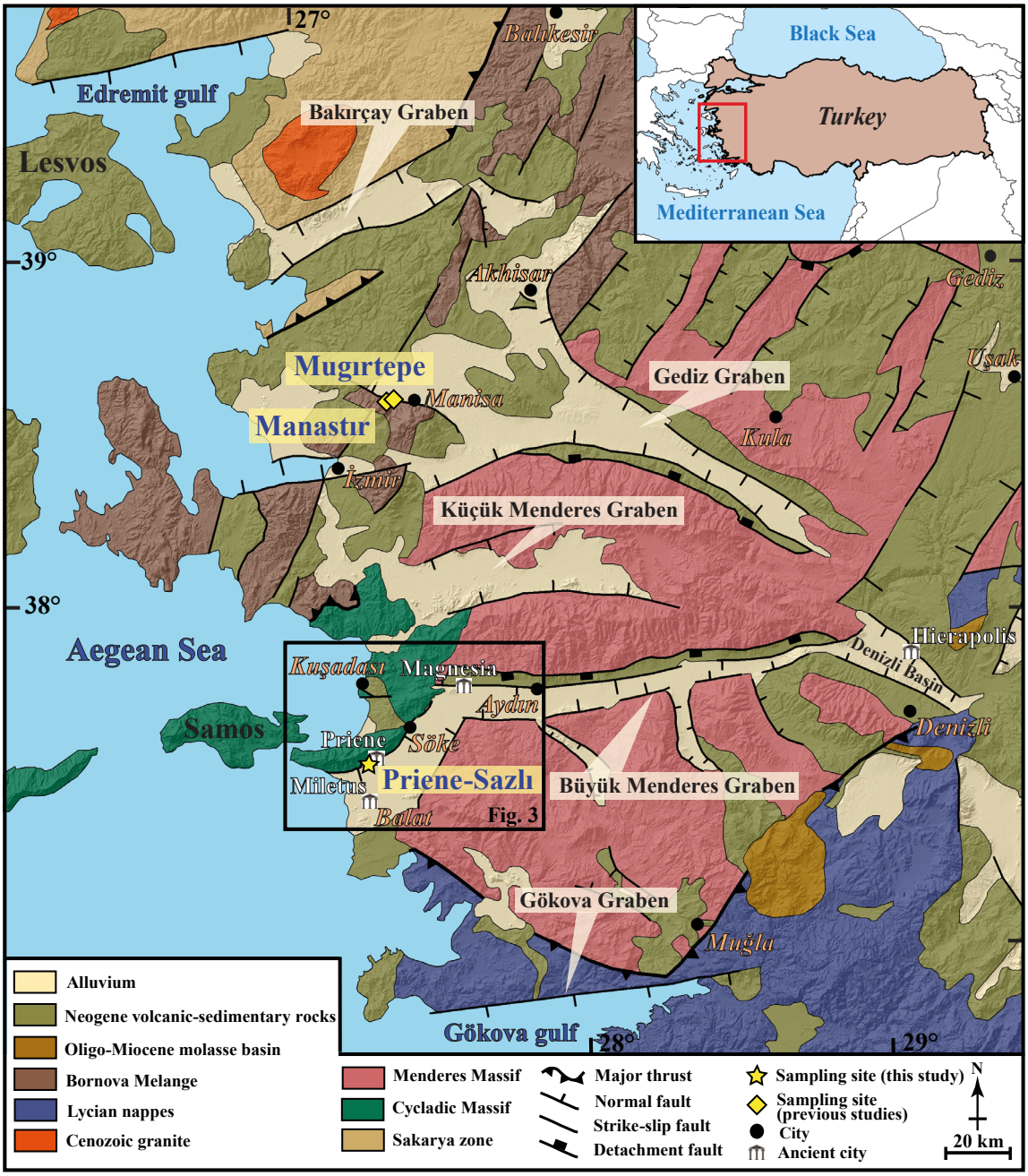

Figure 1. Simplified geological map of Western Anatolia (modified after Hancock and Barka, 1987; Akçar et al., 2012; Sümer et al., 2013). The yellow star shows the location of the sampling site for this study on the Priene–Sazlı Fault. The yellow squares mark the location of the sampling sites on the Mugırtepe Fault (Akçar et al., 2012) and Manastır Fault (Tikhomirov, 2014) within the Manisa Fault Zone. The black box gives the location of Figure 3.

Sümer et al. (2013), the Priene and Sazlıköy segments are probably connected around Söke, even though tracing the segments is difficult due to the overburden of alluvial fan deposits. The longest length suggested for the fault is 40 km (Duman et al., 2011; Emre et al., 2013, 2016). However, in this study we use the surface rupture length of the fault, which is given as 35 km on the active fault map of Turkey (Şaroğlu et al., 1992). The seismogenic depth of the Priene–Sazlı Fault is unknown, but according to a seismic stratigraphic study of the BMG, the faults in this region were traced to a depth of about 12–16 km (Duman et al., 2016), which is interpreted as the transition boundary between the rigid upper crust and the ductile lower crust (Çifçi et al., 2011).

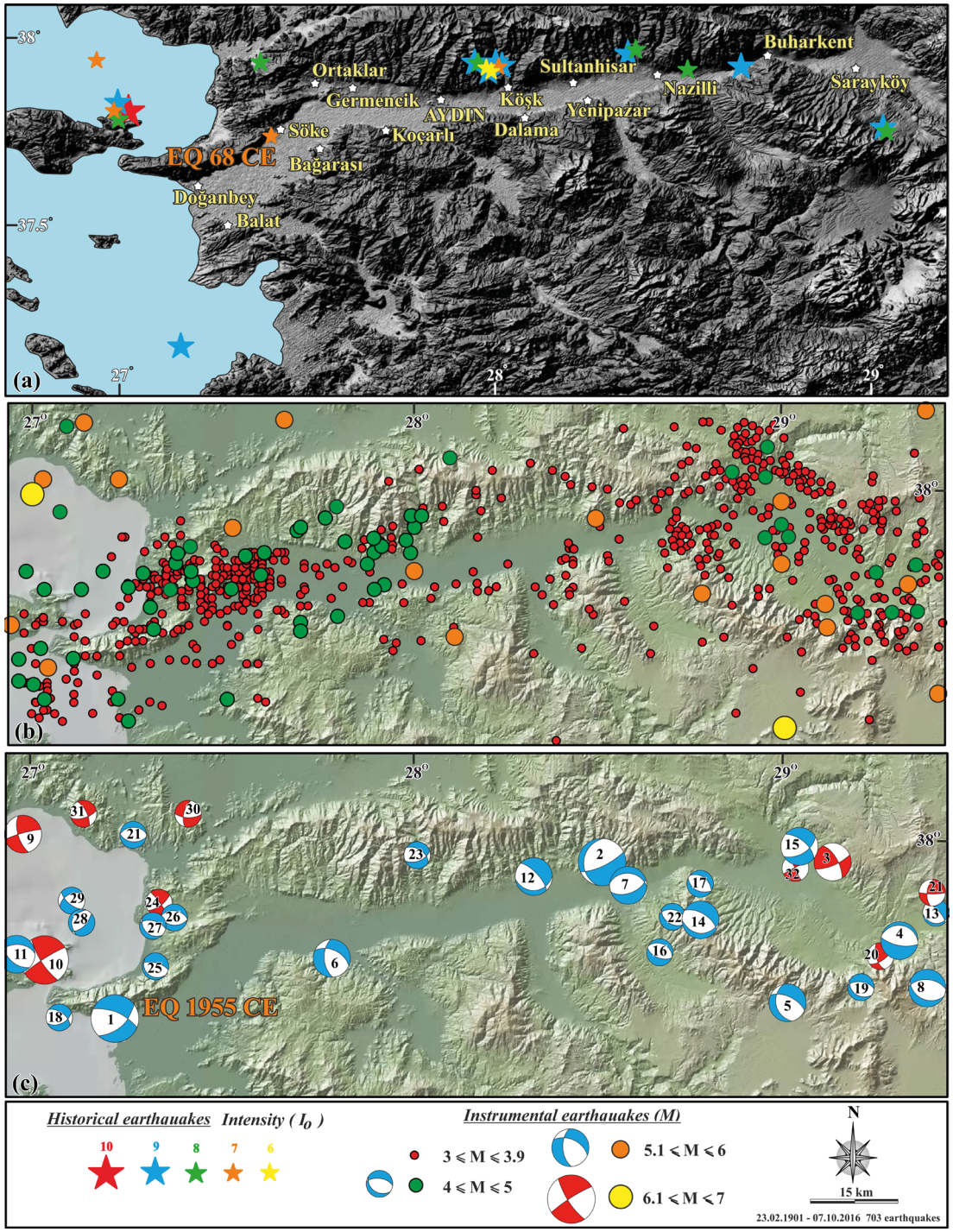

Figure 2. Seismotectonic map of Büyük Menderes Graben and surrounding area showing locations of (a) historical earthquakes (Collection Academique, 1766; Broughton, 1938; Calvi, 1941; Dikmen, 1952; Pınar and Lahn, 1952; Ergin et al., 1967; Öcal, 1968; Karnik, 1971; Shebalin et al., 1974; Ambraseys, 1975; Soysal et al., 1981; Guidoboni et al., 1994; Ambraseys, 2009); (b) instrumental earthquakes; and (c) selected focal mechanism solution (FMS) of the instrumental earthquakes (1, 2, 4: McKenzie, 1972; 3: Canıtez and Üçer, 1967; 5, 6: Kalafat, 1998; 7: Taymaz, 1993; 8, 10, 12, 14, 15, 16: Harvard Centroid Moment Tensor Project CMT, Harvard University, www.globalcmt.org/CMTsearch; 9: Tan and Taymaz, 2001; 11: Tan and Taymaz, 2003; 13: Taymaz et al., 2004; 17, 12: Kalafat et al., 2009; 18, 31: National Observatory of Athens, Greece, bbnet.gein.noa.gr; 19, 22: Istituto Nazionale di Geofisica e Vulcanologia, Italy, http://istituto.ingv.it/; 21, 28, 29, 30: Boğaziçi University Kandilli Observatory and Earthquake Research Institute, koeri.boun.edu.tr/scripts/lst4.asp; 23, 25, 26, 27, 32: Republic of Turkey Prime Ministry Disaster & Emergency Management Presidency-Earthquake Research Department (AFAD-ERD), https://www.afad.gov.tr/en/; 24: United States Geological Survey National Earthquake Information Center, earthquake.usgs.gov/contactus/golden/neic.php).

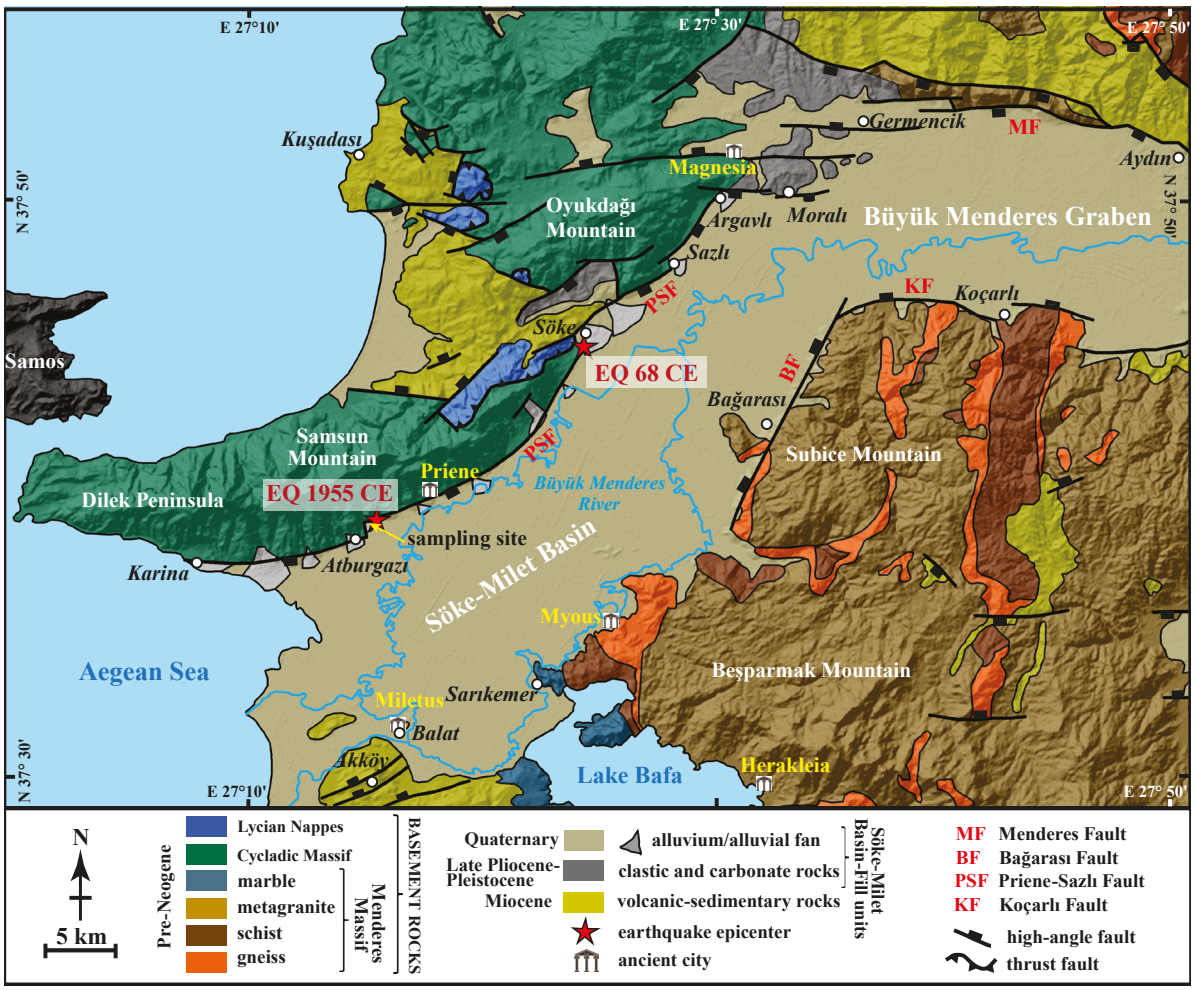

Figure 3. Geological map of the western part of the Büyük Menderes Graben, including location of earthquakes in 68 CE and 1955 CE and the sampling site (modified after Sümer et al., 2012).

In general, the northeastern sections of the Priene–Sazlı Fault segment are structurally characterized by strike-slip striation representing dextral and sinistral movements, which are later overprinted by an oblique-slip normal component (Sümer et al., 2013). The southwestern section of the fault, however, is dominated by dip-slip lineations along with minor dextral movement. These oblique and dip slips are observed along the entire length of the fault segments. Thus, the Priene–Sazlı Fault is a reactivated structure initiated in the Miocene as a dextral strike-slip fault, whose movement later changed to sinistral strike-slip. The fault was reactivated again during the Quaternary as an oblique to dip-slip normal fault (Sümer et al., 2013). The activity on the fault during the Quaternary is proven by development of lateral alluvial fans near Atburgazı in the late Pleistocene, which were intersected and uplifted by the new segment of the fault (e.g., Gürer et al., 2001 and references therein). Near Söke, the fault cut and uplifted the Late Pliocene to Pleistocene sedimentary sequence, which contains an ash layer that is at least 950 ka old, indicating at least one period of activity since the Calabrian (Early Pleistocene) (after Sümer et al., 2012).

The study area includes three main groups of rocks: (1) basement rocks, mainly the Mesozoic Cycladic Massif; (2) Miocene Söke Basin-fill units; and (3) post-Miocene Söke–Milet Basin fill units (Sümer et al., 2012). The Quaternary Söke–Milet Basin constitutes the hanging-wall of the Priene–Sazlı Fault (Figures 3 and 4). The Priene–Sazlı Fault generally juxtaposes the Quaternary sediments of the Söke–Milet Basin with the Cycladic Massif in the footwall, which largely consists of marble and recrystallized limestone (Figure 3).

Two significant seismic events are known to have occurred on the Priene–Sazlı Fault. The first destructive earthquake occurred in 68 CE with an epicenter at the northeastern end of the fault segment, south of Söke, and with an intensity of VII according to the historical records (Ergin et al., 1967) (Figure 3). The second, the Söke–Balat

Figure 4. Field view of the Priene–Sazlı Fault, showing pre-Neogene basement rocks against Söke–Milet Quaternary Basin. Photo was taken from the sampling site.

earthquake, occurred on 16 July 1955 (M = 6.8) (Öcal, 1958). Its epicenter was close to the ancient city of Priene with a focal depth of 7.1 km (Kadirioğlu et al., 2018), similar to the focal depth of the majority of earthquakes that have occurred in this region (Çifçi et al., 2011). In this disaster, 23 people were killed and more than 470 buildings were damaged, mostly in the cities of Söke and Balat (ancient Miletus), 15 km south of ancient Priene (Figure 3).

3. Fault scarp dating

3.1. Background

Fault scarp dating with cosmogenic nuclides has been used during the last two decades to estimate the timing of ruptures that predate the available earthquake archives. ^{36}Cl is the most common cosmogenic nuclide, which is used for dating nonquartz-bearing lithologies such as carbonates. Fault scarp dating with cosmogenic ^{36}Cl was first introduced by Zreda and Noller (1998), with reconstruction of six prehistoric seismic activity ages in the Hebgen Lake fault scarp, Montana, USA. Afterwards, the time-slip histories of limestone fault scarps were modeled in several locations in the Eastern Mediterranean and the Middle East (Mitchell et al., 2001; Benedetti et al., 2002, 2003, 2013; Palumbo et al., 2004; Schlagenhauf et al., 2010, 2011; Akçar et al., 2012; Mouslopoulou et al. 2014; Tikhomirov, 2014; Tesson et al., 2016; Cowie et al., 2017; Beck et al., 2018; Mechernich et al., 2018). In addition, ^{10}Be, ^{14}C, and ^{26}Al cosmogenic nuclides were tested for dating of fault scarps (Harrington et al., 2000; Kong et al., 2010).

Mitchell et al. (2001) modeled three distinct periods of paleoseismic activity using cosmogenic ^{36}Cl surface fault-scarp dating on the Nahef East Fault scarp, Israel. Benedetti et al. (2002) studied the Sparta Normal Fault scarp (Greece) and reconstructed six seismic events including the 464 BCE Sparta earthquake. Furthermore, Benedetti et al. (2003) identified three rupture events on the Kaparelli Fault, Greece, that occurred between 10 and 20 ka. Palumbo et al. (2004) reported five to seven seismic ruptures during the last 12 ka at one site on the Mangola Fault, Italy. Schlagenhauf et al. (2010) developed a new MATLAB code and reprocessed the cosmogenic ^{36}Cl data from the Mangola Fault (Palumbo et al., 2004). They discovered the same number of events as Palumbo et al. (2004), but determined the events to be younger by about 3–5 ka. Schlagenhauf et al. (2011) sampled four additional sites on the Velino–Magnola Fault and reconstructed an age-slip history of a minimum of nine major ruptures over the last 15 ka based on the results from the five sites (including one from Palumbo et al., 2004). Akçar et al. (2012) applied the MATLAB code of Schlagenhauf et al. (2011) to the Mugırtepe Fault in the Manisa Fault Zone, Turkey to model measured cosmogenic ^{36}Cl (Figure 1). They proposed two scenarios for the exposure of the fault, including one or two seismic event(s). Benedetti et al. (2013) identified more than 30 major earthquakes over the last 12 ka on the Fucino Fault System, Italy, based on cosmogenic ^{36}Cl measurements from 11 sites, including one site studied by Palumbo et al. (2004) and four studied by Schlagenhauf et al. (2011). Tikhomirov (2014) developed a new MATLAB code and reanalyzed the results from the Mugırtepe Fault (Akçar et al., 2012) and the Manastır Fault in the Manisa Fault Zone (Figure 1). The new modeling resulted in one rupture for each fault. Mouslopoulou et al. (2014) applied the code of Schlagenhauf et al. (2011) to the Spili Fault (Crete) and reconstructed five major rupture events over the last 16.5 ka. Tesson et al. (2016) applied the same code and recovered a minimum of six past earthquakes in the period of 3 ka to 1 ka on the Pizzalto Fault, Italy. Cowie et al. (2017) combined cosmogenic ^{36}Cl dating with LiDAR and GRP methods to reconstruct the slip history of the Italian Apennines over the last 18 ka and found episodic activity on the Fiamignano Fault. Mechernich et al. (2018)

explored at least six seismic events on the Pisia Fault, Greece, during the last 7.3 ka following Schlagenhauf et al. (2010). Beck et al. (2018) proposed a Bayesian MATLAB code, an improved version of that of Schlagenhauf et al. (2010) and Cowie et al. (2017), to determine displacement on the Fiamignano and Frattura faults, Italy.

Fault scarp dating analyzes the cosmogenic ^{36}Cl concentration along the fault scarp surface, namely in the uppermost few centimeters. The variation of cosmogenic ^{36}Cl is shaped by successive displacements and episodes of quiescence (Figure 5) (Zreda and Noller, 1998). The analysis of cosmogenic ^{36}Cl along the fault scarp enables the dating of past ruptures and estimation of the recurrence period of the earthquakes, the determination of the vertical component of slip and the magnitude of the past earthquakes, and the estimation of the long-term and short-term slip rates, which are essential parameters for earthquake hazard analysis (e.g., Cluff and Cluff, 1984).

During the dormancy period prior to a rupture, the shielding effect of colluvium causes an exponential decrease in ^{36}Cl concentration along the footwall surface below point G in Figure 5a. The time when the fault was totally covered by colluvium is shown as t_0 in Figure 5b. Once rupture occurs (at time t_1), the faulting exposes a previously buried section of the scarp with slip S_1 and the colluvium position shifts from position G_0 to G_1 (Figure 5b, EQ_1); this leads to a uniform accumulation of cosmogenic ^{36}Cl in this section at a higher rate through the consequent periods of quiescence (time span of t_1 to t_2, where t_2 is timing of the second earthquake). Then the second earthquake (EQ_2) occurs at time t_2 with a slip of S_2 and the ground level moves from position G_1 to G_2. This cycle repeats for the third and fourth earthquakes, after which the ground level shifts to G, which is the recent ground level (Figure 5b). Hence, each discontinuity in the profile of ^{36}Cl concentrations accumulated during these four earthquakes marks the timing of a single rupture. Convex patterns on the ^{36}Cl profile along the fault scarp indicate phases of inactivity (Figure 5b). The vertical separation between two successive discontinuities equates to the respective slip of the rupture (Figure 5b).

3.2. Sampling

In normal faults, vertical displacement is not uniform along the entire fault strike (e.g., Walsh and Watterson,

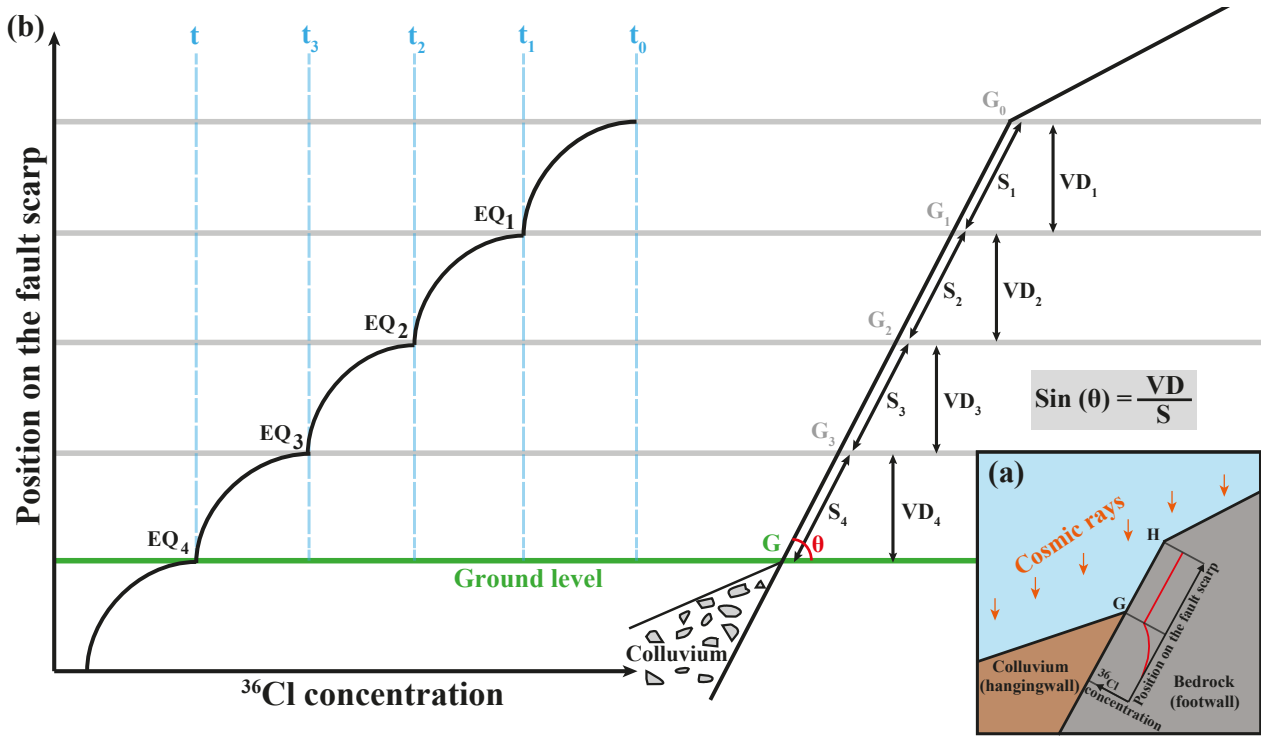

Figure 5. (a) Schematic distribution of cosmogenic ^{36}Cl concentration along an exposed fault scarp and surface covered by colluvium; (b) sketch of cosmogenic ^{36}Cl concentration profile as a function of height along the fault scarp through exposure history of four episodic earthquakes (modified after Akçar et al., 2012). G_0 and t_0 represent the ground level and time before the first earthquake, when the fault was covered by colluvium; G_1 and S_1 show the ground level and the slip value after the first earthquake at the time of t_1; t is the time of the fourth and most recent earthquake, when ground level shifted from G_3 to its current level (G); S_4 represents slip amount of the last earthquake. The differences between adjacent times of t_0 to t indicate inactive periods on the fault; VD_1 to VD_4 are vertical displacement caused by earthquakes 1 to 4.

1988; Marrett and Allmendinger, 1991). Based on our field observations, the Priene–Sazlı Fault has the highest vertical displacement in the center of its strike, whereas it decreases to zero towards the tips, similar to the majority of normal faults. In such circumstances, the displacement pattern follows an approximately elliptical contour with the short axis parallel to the displacement and the long axis parallel to the fault strike (Barnett et al., 1987; Walsh and Watterson, 1987; Walsh et al., 2003; Kim and Sanderson, 2005) (Figure 6). Therefore, in similar conditions an appropriate sampling site for cosmogenic ^{36}Cl analysis is a clear and smooth surface around the center of the fault scarp. Although there are studies opposing this idea (Bubeck et al., 2015; Manighetti et al., 2015; DuRoss et al., 2016; Perrin et al., 2016), the aforesaid models are in concordance with our field observations.

In order to model at least one past rupture using the analysis of cosmogenic ^{36}Cl, the vertical extent of the exposed fault scarp from which samples is collected should be a minimum of 2 m above ground level (e.g., Tikhomirov, 2014). Ideally, a continuous strip parallel to the vertical slip vector is sampled. However, a series of laterally shifted strips can be also sampled (e.g., Benedetti et al., 2002; Schlagenhauf et al., 2011; Akçar et al., 2012), where there is clear evidence for minimum weathering and erosion (Tikhomirov, 2014).

First, we identified potential sites for sampling along the Priene–Sazlı Fault and we selected the sampling surface after a reconnaissance study. According to our field observations this section shows the highest cumulative displacement along the entire length of the fault. Furthermore, this section of the fault is the most uplifted part geomorphologically with a height of about 200 m. Following these criteria, we sampled a well-exposed portion of the scarp surface (trending N60°E and dipping to 50°–55° SE) in the lowermost part of the Priene–Sazlı Normal Fault in Atburgazı village (Figure 7a). This surface has minimal weathering and erosion along the center of the fault strike, close the maximum slip (Figures 7 and 8). The lower part of the fault was covered by colluvium with a dip of ca. 20° extending towards the Söke–Milet basin (Figure 7b). We marked four sampling strips (A–D), with a total vertical relief of ca. 12 m (Figures 7b and 7c) and parallel to the dip-slip lineation on the fault surface. This young phase of lineation is representative of reactivation of the fault during the Quaternary (Sümer et al., 2013). A total of 117 slabs of 15 cm wide and 10 cm high were cut using a hand-held diamond saw. From the 7.3-m-long strip A, 73 slabs were collected as the main strip (Figure 7d), while the remaining 44 slabs were collected from strips B, C, and D. Afterwards, the slabs were removed using a chisel and hammer (Figure 7d).

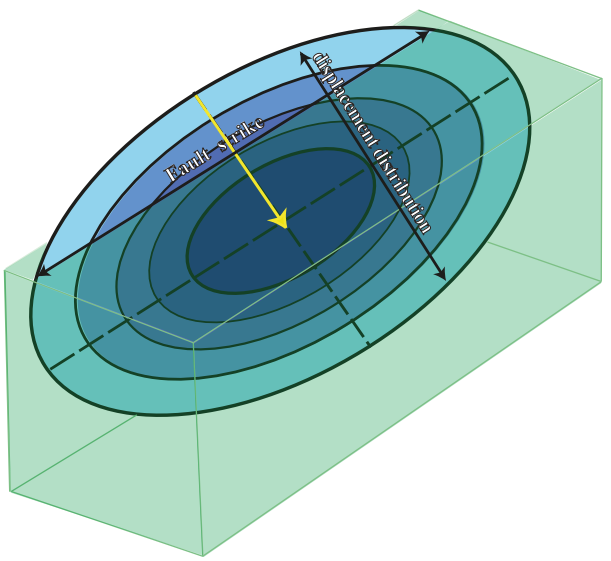

Figure 6. Schematic cartoon of normal fault illustrating displacement distribution on an elliptical fault pattern, which has a maximum in the center of the fault strike (modified after Kim and Sanderson, 2005). The short axis of elliptical isolines is parallel to displacement and the long axis is parallel to the fault strike.

The geometry of the fault scarp strongly defines the shape of the modeled concentration profile. Hence, geometric parameters are important for precise dating of the fault scarp. The main parameters of the scarp geometry required to model the rupture history are: (1) scarp dip (the angle between the fault scarp surface and horizontal plane), (2) scarp height (height of the fault scarp surface from the ground level to the top edge), (3) top surface dip (angle between upper part of the fault scarp and the horizontal plane), and (4) colluvium dip (angle between colluvium surface of about 15 m from the fault surface and horizontal plane) (e.g., Schlagenhauf et al., 2010; Tikhomirov, 2014) (Figure 7e). During our fieldwork, the exact position of each sample was measured relative to the ground level. Topographic shielding was defined as obstacles around the scarp including mountains, ridges, and higher scarps. In addition, the density of colluvium was measured with a bucket of ca. 19,800 cm^3 volume, ca. 30,000 g of colluvium, and a balance in the field.

3.3. Cosmogenic ^{36}Cl analysis

The samples were prepared at the Surface Exposure Dating Laboratory of the University of Bern according to the procedure introduced by Stone et al. (1996) and Ivy-Ochs et al. (2004, 2009), based on the isotope dilution technique (Elmore et al., 1997; Ivy-Ochs et al., 2004; Desilets et al., 2006). The collected slabs were cut parallel to the surface to a maximum thickness of 3 cm. The samples were then crushed and sieved into the fraction of 0.25–0.4 mm. Thereafter, any metal chips remaining from the grinding

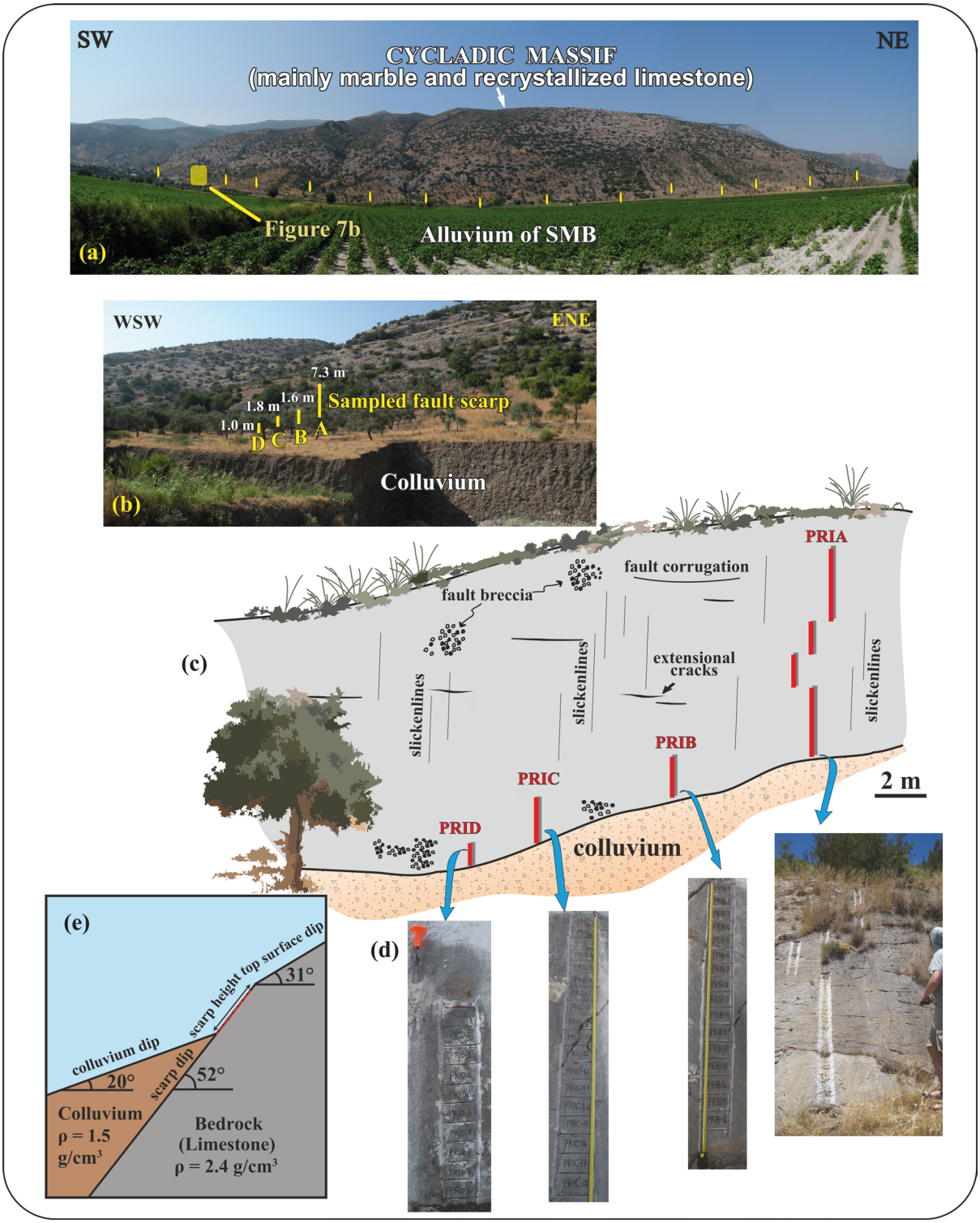

Figure 7. (a) Field view of the Priene–Sazlı Fault scarp at the base of the escarpment. (b) More detailed view of fault scarp with positions of continuous sampled strips A, B, C and D. The sampled surface is the lowest exposed surface of the successive scarp system. (c) Schematic sketch of fault scarp surface representing four sampled strips. (d) Fault scarp surface showing sampling slabs along strips A, B, C, and D. (e) Schematic sketch showing important parameters of the fault scarp for modeling, including scarp height, scarp dip, colluvium dip, top surface dip, and density of the bedrock and colluvium. Red dashed line shows the sampled surface.

Figure 8. The sampled surface of the Priene–Sazlı Fault scarp.

material were removed with a hand magnet. In order to remove Cl that was not in situ (Zreda et al., 1991), the crushed material was leached in 75 mL of 2 M HNO_3 overnight and then rinsed four times with ultrapure water (18.2 MΩ cm). Leaching was repeated a second time. The samples were then dried on a hotplate at 60 °C. Aliquots of about 12 g from each of 10 samples as representative samples were analyzed for major and trace elements by inductively coupled plasma mass spectrometry at SGS Mineral Services, Toronto, Canada. In addition, the Ca content was determined for each sample individually.

Afterwards, batches of a maximum of 16 samples along with one full process blank were processed. Samples were spiked with about 2.5 mg of ultrapure ^{35}Cl to determine the amount of total Cl concentration (^{35}Cl, ^{37}Cl) (Ivy-Ochs et al., 2004, 2009) and dissolved with HNO_3. Determination of the total Cl concentration is required in order to calculate the ^{36}Cl concentration in the sample from the accelerator mass spectrometry (AMS)-measured $^{36}Cl/Cl$ ratio, the ^{36}Cl production from ^{35}Cl by low-energy neutron capture, and the noncosmogenic subsurface production of ^{36}Cl (Ivy-Ochs et al., 2004). The samples were centrifuged to separate impurities. In the dark, 10 mL of $AgNO_3$ was added to the supernatant at 200 °C to precipitate AgCl. Then the precipitated AgCl was collected and dissolved with 2 mL of NH_4OH. The samples were centrifuged to eliminate cations. $BaSO_4$ was precipitated by addition of $Ba(NO_3)_2$ to the supernatant in order to avoid interference of the ^{36}S isobar with ^{36}Cl during the AMS measurements. Finally, the AgCl decant was recovered as a solid, rinsed with ultrapure water, and dried. AgCl samples were pressed into targets for AMS measurements.

The concentrations of total Cl and ^{36}Cl were measured from a single target at the ETH (Eidgenössische Technische Hochschule) AMS facility following the isotope dilution technique (Synal et al., 1997; Ivy-Ochs et al., 2004; Christl et al., 2013), which results in increasing precision and sensitivity of the ^{36}Cl measurement (Ivy-Ochs et al., 2004; Desilets et al., 2006). The stable ratio of $^{37}Cl/^{35}Cl$ was normalized to the neutral ratio $^{37}Cl/^{35}Cl$ = 31.98% of the K382/4N standard and the machine blank, whereas sample ratios of $^{36}Cl/^{35}Cl$ were normalized to the ETH internal standard K382/4N with $^{36}Cl/Cl = (17.36 \pm 0.35) \times 10^{-12}$ (Christl et al., 2013). The sulfur correction of measured $^{36}Cl/^{35}Cl$ ratios was negligible. In addition, $^{36}Cl/^{35}Cl$ ratios of the measured samples were corrected for a procedure blank of $(1 \pm 0.02) \times 10^{-15}$, which amounted to a correction of less than 1% for the samples.

3.4. Data analysis software

We carried out an analysis of the Priene–Sazlı Fault dataset with the FSDT forward modeling MATLAB code (provided as supplementary material; after Tikhomirov, 2014). The code applies the fault scarp shielding model to calculate the ^{36}Cl accumulation, a two-step approximation to reconstruct a particular rupture history, and the Monte Carlo method to search for the most realistic rupture

history. Rupture histories are randomly generated in bounded solution space and evaluated with statistical tests to compare the measured and modeled ^{36}Cl profiles.

Reconstruction of the exposure history of a fault scarp is performed in two stages (Tikhomirov, 2014). In the first stage, distributions of particle fluxes are precisely calculated at the nodes of a 3D mesh, which covers all possible positions of the sample strip. The program automatically saves the results of the first stage, which is used as a database for the second stage of calculations. During the second stage, database fluxes are interpolated to represent a given exposure history of the fault scarp, and the concentration profile of accumulated cosmogenic ^{36}Cl is calculated. All production pathways for cosmogenic ^{36}Cl, such as high-energy neutrons, fast and negative muons, and thermal and epithermal neutrons (Liu et al., 1994; Phillips et al., 1996, 2001; Stone et al., 1996, 1998; Alfimov and Ivy-Ochs, 2009; Schimmelpfennig et al., 2009), are accounted for by the FSDT code. We used the following production rates of ^{36}Cl by high-energy neutron spallation of 48.8 ± 3.4 at g^{-1} $year^{-1}$ on Ca (Stone et al., 1996), 170 ± 25 at g^{-1} $year^{-1}$ on K (Evans et al., 1997), 13 ± 3 at g^{-1} $year^{-1}$ on Ti (Fink et al., 2000), and 1.9 ± 0.2 at g^{-1} $year^{-1}$ on Fe (Stone, 2005). The production rate of epithermal neutrons from fast neutrons in the atmosphere at the land/atmosphere interface of 760 ± 150 n g^{-1} $year^{-1}$ was used (Alfimov and Ivy-Ochs, 2009). In order to scale to the local production rates, we applied the scaling factors of Stone (2000) for a constant geomagnetic field. Besides the production rates, an analysis with the FSDT code requires scarp geometry, topographic shielding, and the chemical composition of each sample and colluvium, as well as thickness and position of each sample. Furthermore, the beginning of exposure and the erosion rate are important parameters that can be determined using a mean value along with standard deviation to bound the solution space for further runs. The beginning of exposure is considered to be the theoretical age when production of ^{36}Cl in the sample strip became appreciable. The erosion rate value is limited by the maximal total erosion value in the database, which we normally define as 15 cm/ka, and by the age of sample strip exposure. Modeled rupture histories are automatically generated in a bounded solution space with the Monte Carlo method.

In the initial runs, a wide solution space in terms of various scenarios with different numbers of rupture events, ages, and associated slips is also manually applied. The chi-square threshold can be set either by the user or automatically to represent a given confidence window. The modeled and measured ^{36}Cl profiles are compared using statistical tests of chi-square (c^2), weighted root mean square (RMSw), and Akaike information criterion (AICc), which are computed for each rupture history. In later simulations, the solution space is narrowed around the most probable values. Finally, the scenario with the lowest c^2 and AICc values is accepted as the most probable solution.

Since the majority of the previous publications on fault scarp dating with ^{36}Cl used the methodology proposed by Schlagenhauf et al. (2010), we would like to highlight the major differences between the Schlagenhauf and FSDT models. The models of cosmic ray shielding by the fault scarp of the two codes were compared by Tikhomirov et al. (2014). The FSDT code applies scarp shielding to all cosmogenic particles producing ^{36}Cl, including neutron spallation, fast muons, and thermal and epithermal neutrons. In contrast, the Schlagenhauf code applies scarp shielding only to neutron spallation. It also uses one exponential simplification of muon attenuation, while FSDT uses the full model published by Heisinger et al. (2002a, 2002b). These differences between the models can yield a discrepancy of a few percentages, depending on the circumstances in the results. In addition to having a more accurate model of the interaction of secondary cosmic rays with matter, the FSDT code conducts an extensive search for the optimal solution with the Monte Carlo method. Both programs use forward modeling, but the FSDT code applies a precalculated database and two-step approximation, which significantly reduces computation time for the ^{36}Cl profile based on a particular fault scarp history. Our program will be published in a separate article, in conjunction with an error propagation code.

4. Results

The position of the samples along the fault scarp, the sample thickness, the cosmogenic ^{36}Cl concentration and its uncertainty, and the natural chlorine concentration, as well as calcium, oxygen, and carbon concentrations, are listed in Tables 1–4 for sampling strips A, B, C, and D, respectively. Major and trace element concentrations of 14 representative samples from the fault scarp and averaged values used for modeling are given in Table 5. The fault scarp parameters are shown in Table 6. The density of colluvium was measured as 1.5 g/cm^3 in the field and the density of the scarp is considered to be 2.4 g/cm^3. The amounts of sample material and spike used for all ^{36}Cl samples and ^{37}Cl/^{35}Cl and ^{36}Cl/^{35}Cl ratios along with uncertainties are provided in Appendix A.

Measured cosmogenic ^{36}Cl concentrations and their 1σ errors are plotted as a function of height within each strip (Figure 9). The concentration of cosmogenic ^{36}Cl varies between 0.918 (±0.052) × 10^5 at g^{-1} to 3.558 (±0.133) × 10^5 at g^{-1} along the strips (Figure 9). Cosmogenic ^{36}Cl concentrations along the fault scarp in strip A generally show a clear logarithmic increase with height (Figure 9a), while they vary almost within 1σ in strips B, C, and D (Figures 9b, 9c, and 9d).

Table 1. Stable Cl, cosmogenic ^{36}Cl and calcium concentrations, thickness, and top and bottom position of the samples from strip A of the Priene–Sazlı scarp.

Sample name	Top position, cm	Bottom position, cm	Thickness, cm	^{36}Cl*, 10^5 at/g	^{36}Cl uncertainty*, 10^5 at/g	Cl_{total}*, ppm	Cl_{total} uncertainty*, ppm	Ca…, ppm
PRI-A01	732	722	2.0	3.558	0.133	6.1	0.06	360205
PRI-A02	722	712	2.0	3.070	0.139	9.7	0.10	353058
PRI-A03	712	702	2.5	3.036	0.089	9.1	0.09	348056
PRI-A04	702	692	2.0	2.950	0.132	9.6	0.10	344482
PRI-A05	692	682	2.0	2.871	0.126	13.6	0.14	367352
PRI-A06	682	672	2.0	2.922	0.133	14.8	0.15	363064
PRI-A07	672	662	3.0	2.628	0.091	4.9	0.05	378073
PRI-A08	662	652	2.5	2.411	0.098	6.3	0.06	368782
PRI-A09	652	642	2.0	2.479	0.110	10.0	0.10	379502
PRI-A10	642	632	2.0	2.685	0.098	15.5	0.15	380217
PRI-A11	632	622	2.0	2.411	0.105	11.2	0.11	367352
PRI-A12	622	612	2.5	2.436	0.087	7.3	0.07	373785
PRI-A13	612	602	3.0	2.586	0.115	8.6	0.09	368782
PRI-A14	602	592	3.0	2.521	0.102	4.4	0.04	380217
PRI-A15	592	582	2.5	2.360	0.108	2.6	0.03	375214
PRI-A16	582	572	2.0	2.536	0.115	4.4	0.04	354488
PRI-A17	572	562	2.0	2.402	0.083	4.7	0.05	366638
PRI-A18	562	552	2.5	2.367	0.098	2.0	0.02	380932
PRI-A19	552	541	2.5	2.705	0.118	3.6	0.04	376643
PRI-A20	541	531	5.0	2.397	0.105	7.0	0.07	369496
PRI-A21	531	521	2.5	2.591	0.134	8.4	0.08	365923
zPRI-A22	521	511	2.0	2.313	0.087	7.6	0.08	368782
PRI-A23	511	501	2.0	2.250	0.119	7.6	0.08	351629
PRI-A24	501	491	2.5	2.180	0.118	7.4	0.07	358061
PRI-A25	491	481	2.5	2.077	0.093	6.7	0.07	353773
PRI-A26	481	471	2.0	2.382	0.111	7.2	0.07	359491
PRI-A27	471	461	2.0	1.919	0.076	8.6	0.09	363064
PRI-A28	461	451	2.0	2.177	0.107	10.1	0.10	355917
PRI-A29	451	441	2.5	2.162	0.119	2.6	0.03	369496
PRI-A30	441	431	2.0	2.121	0.082	2.7	0.03	381646
PRI-A31	431	421	2.5	2.192	0.093	3.4	0.03	385220
PRI-A32	421	411	2.0	2.088	0.079	7.0	0.07	382361
PRI-A33	411	401	2.5	2.171	0.091	8.8	0.09	362350
PRI-A34	401	391	2.0	2.208	0.104	4.8	0.05	382361
PRI-A35	391	381	2.5	2.033	0.085	5.1	0.05	371641
PRI-A36	381	371	2.0	2.229	0.112	12.6	0.13	349485
PRI-A37	371	361	2.0	1.791	0.079	12.3	0.12	358061
PRI-A38	361	351	2.0	1.821	0.097	12.4	0.12	372355
PRI-A39	351	341	2.0	1.526	0.086	8.8	0.09	365923
PRI-A40	341	331	2.0	1.843	0.081	7.0	0.07	363779
PRI-A41	331	321	2.0	1.797	0.097	6.5	0.06	348056

Table 1. (Continued).

PRI-A42	321	311	2.0	1.524	0.067	4.3	0.04	335906
PRI-A43	311	301	2.0	1.839	0.093	4.8	0.05	330188
PRI-A44	301	291	2.0	1.815	0.097	6.1	0.06	357347
PRI-A45	291	281	2.0	1.771	0.087	8.3	0.08	358776
PRI-A46	281	271	2.0	1.804	0.092	7.3	0.07	360205
PRI-A47	271	261	2.0	1.599	0.061	6.4	0.06	348770
PRI-A48	261	251	2.5	1.672	0.093	7.9	0.08	350914
PRI-A49	251	241	1.5	1.742	0.102	7.6	0.08	365923
PRI-A50	241	231	2.0	1.744	0.079	7.2	0.07	363064
PRI-A51	231	221	2.5	1.493	0.097	4.8	0.05	330903
PRI-A52	221	211	2.0	1.316	0.054	4.2	0.04	358776
PRI-A53	211	201	2.0	1.510	0.095	2.8	0.03	357347
PRI-A54	201	191	2.5	1.681	0.075	2.9	0.03	358776
PRI-A55	191	180	2.5	1.328	0.066	4.0	0.04	345197
PRI-A56	180	170	2.0	1.317	0.063	4.6	0.05	328759
PRI-A57	170	160	2.0	1.394	0.065	3.6	0.04	343053
PRI-A58	160	150	2.0	1.280	0.058	2.6	0.03	353773
PRI-A59	150	140	2.0	1.659	0.081	2.8	0.03	339479
PRI-A60	140	130	2.0	1.313	0.068	1.7	0.02	355203
PRI-A61	130	120	2.5	1.357	0.065	2.3	0.02	355203
PRI-A62	120	110	1.5	1.179	0.056	3.9	0.04	345197
PRI-A63	110	100	2.0	1.222	0.066	4.1	0.04	350914
PRI-A64	100	90	2.0	1.340	0.060	8.0	0.08	367352
PRI-A65	90	80	3.0	1.166	0.074	4.6	0.05	332332
PRI-A66	80	70	2.0	1.127	0.051	4.7	0.05	325900
PRI-A67	70	60	2.0	0.928	0.068	6.1	0.06	295883
PRI-A68	60	50	2.0	1.083	0.047	5.0	0.05	325185
PRI-A69	50	40	2.0	1.058	0.052	3.8	0.04	343053
PRI-A70	40	30	2.0	1.126	0.059	6.6	0.07	357347
PRI-A71	30	20	1.5	1.170	0.056	10.1	0.10	372355
PRI-A72	20	10	2.5	1.268	0.065	9.5	0.09	368067
PRI-A73	10	0	2	1.154	0.060	6.8	0.07	373785

*Measured with accelerator mass spectrometry (AMS).
…Measured with ICP95A at SGS Mineral Services, Canada.

The probability density functions (PDFs) for cosmogenic ^{36}Cl normalized to Ca concentrations for strips A, B, C, and D are plotted in Figure 10. The PDF plot of strip A detects nonlinear ^{36}Cl distributions, in which vertical dashed lines mark maximum probability density indicating three notable peaks at heights of about 100, 250, and 550 cm along the fault scarp (Figure 10a). In strips B, C, and D, concentrations of cosmogenic ^{36}Cl along the scarp height form only one peak in each PDF plot (Figures 10b, 10c, and 10d).

For modeling of the paleoseismic history of the Priene–Sazlı Fault, first we examined simulations based on six databases involving the combined strips ABCD and BCD, as well as each strip A, B, C, and D, individually. Then we ran the code with various rupture scenarios in terms of constraining the number of earthquakes, the age of the earthquakes, slip amounts, and erosion rates. The best-fit solution for each scenario based on different datasets is summarized in Table 7. Since the simulation of earthquakes based on strip A showed the best distributions

Table 2. Stable Cl, cosmogenic ^{36}Cl and calcium concentrations, thickness, and top and bottom position of the samples from strip B of the Priene–Sazlı scarp.

Sample name	Top position, cm	Bottom position, cm	Thickness, cm	^{36}Cl*, 10^5 at/g	^{36}Cl uncertainty*, 10^5 at/g	Cl_{total}*, ppm	Cl_{total} uncertainty*, ppm	Ca…, ppm
PRI-B01	160	150	2.0	1.362	0.069	7.7	0.08	380932
PRI-B02	150	140	2.0	1.254	0.066	6.6	0.07	380932
PRI-B03	140	130	1.5	1.270	0.073	6.2	0.06	388793
PRI-B04	130	120	2.0	1.194	0.066	6.1	0.06	389508
PRI-B05	120	110	3.0	1.337	0.085	6.2	0.06	388078
PRI-B06	110	100	1.5	1.198	0.076	4.7	0.05	384505
PRI-B07	100	90	2.0	1.374	0.069	5.5	0.06	395225
PRI-B08	90	80	2.5	1.348	0.068	4.9	0.05	392367
PRI-B09	80	70	2.0	1.224	0.072	5.1	0.05	386649
PRI-B10	70	60	2.5	1.133	0.064	6.1	0.06	371641
PRI-B11	60	50	2.0	1.210	0.066	4.6	0.05	373785
PRI-B12	50	40	2.0	1.138	0.058	4.6	0.05	379502
PRI-B13	40	30	2.0	1.350	0.078	4.4	0.04	381646
PRI-B14	30	20	2.0	1.043	0.061	4.3	0.04	384505
PRI-B15	20	10	3.0	1.255	0.074	4.6	0.05	385934
PRI-B16	10	0	2.0	1.017	0.053	3.9	0.04	380932

*Measured with accelerator mass spectrometry (AMS).
…Measured with ICP95A at SGS Mineral Services, Canada.

Table 3. Stable Cl, cosmogenic ^{36}Cl and calcium concentrations, thickness, and top and bottom position of the samples from strip C of the Priene–Sazlı scarp.

Sample name	Top position, cm	Bottom position, cm	Thickness, cm	^{36}Cl*, 10^5 at/g	^{36}Cl uncertainty*, 10^5 at/g	Cl_{total}*, ppm	Cl_{total} uncertainty*, ppm	Ca…, ppm
PRI-C01	179	169	2.0	1.181	0.062	9.0	0.09	324471
PRI-C02	169	159	2.0	1.272	0.059	8.3	0.08	330903
PRI-C03	159	149	3.0	1.287	0.067	6.6	0.07	351629
PRI-C04	149	139	2.0	1.344	0.078	7.1	0.07	335191
PRI-C05	139	129	2.0	1.155	0.061	9.1	0.09	326615
PRI-C06	129	119	2.0	1.261	0.058	9.0	0.09	331618
PRI-C07	119	109	3.0	1.227	0.056	7.3	0.07	338050
PRI-C08	109	100	2.0	1.243	0.076	8.4	0.08	340909
PRI-C09	100	90	2.0	1.096	0.056	10.4	0.10	344482
PRI-C10	90	80	2.0	1.111	0.050	7.5	0.07	335906
PRI-C11	80	70	2.0	1.111	0.056	7.1	0.07	336621
PRI-C12	70	60	2.0	1.329	0.079	8.0	0.08	357347
PRI-C13	60	50	2.0	1.205	0.055	7.6	0.08	354488
PRI-C14	50	40	2.0	1.258	0.050	6.7	0.07	360205
PRI-C15	40	30	2.0	1.176	0.060	5.7	0.06	383790
PRI-C16	30	20	2.0	1.060	0.052	9.0	0.09	383076
PRI-C17	20	10	2.0	1.281	0.059	11.5	0.11	385220
PRI-C18	10	0	2.0	1.119	0.063	6.0	0.06	380932

*Measured with accelerator mass spectrometry (AMS).
…Measured with ICP95A at SGS Mineral Services, Canada.

Table 4. Stable Cl, cosmogenic ^{36}Cl and calcium concentrations, thickness, and top and bottom position of the samples from strip D of the Priene–Sazlı scarp.

Sample name	Top position, cm	Bottom position, cm	Thickness, cm	^{36}Cl*, 10^5 at/g	^{36}Cl uncertainty*, 10^5 at/g	Cl_{total}*, ppm	Cl_{total} uncertainty*, ppm	Ca…, ppm
PRI-D01	102	91	2.5	1.171	0.053	12.3	0.12	350914
PRI-D02	91	81	2.0	1.161	0.067	9.6	0.10	352344
PRI-D03	81	71	2.5	1.241	0.060	25.8	0.26	362350
PRI-D04	71	61	2.0	1.279	0.079	30.9	0.31	373785
PRI-D05	61	51	3.0	1.177	0.067	20.7	0.21	363779
PRI-D06	51	41	2.0	1.111	0.057	13.5	0.13	345912
PRI-D07	41	30	2.5	1.081	0.066	20.7	0.21	345912
PRI-D08	30	20	1.5	1.101	0.066	19.8	0.20	347341
PRI-D09	20	10	2.0	0.918	0.052	18.7	0.19	330188
PRI-D10	10	0	2.0	0.987	0.061	19.2	0.19	333762

*Measured with accelerator mass spectrometry (AMS).
…Measured with ICP95A at SGS Mineral Services, Canada.

and lowest statistical criteria regarding the number of samples, we focused on three scenarios from strip A.

The known earthquakes of 68 CE and 1955 CE were given as independent input parameters for the modeled five- and six-earthquake scenarios. However, the value of modeled slip for the youngest event fitted to the 1955 CE earthquake was either zero or negligible in all runs (Table 7). In all examined scenarios associated with strip A, the slip value of the oldest modeled earthquake was higher than the subsequent slips. Among these scenarios, the scenario of four earthquake events showed the best fit with the beginning of exposure at ca. 21 ka. The ages of the four earthquake events are 8.1 ± 2.0 ka, 6.0 ± 1.5 ka, 3.7 ± 0.9 ka, and 2.2 ± 0.5 ka with vertical components of associated slip of 3.4 ± 0.5 m, 1.5 ± 0.2 m, 1.4 ± 0.2 m, and 1.5 ± 0.2 m, respectively (Figures 11 and 12). The distances between ruptures indicate mean values of vertical slip rates of more than 0.3, 0.7, 0.6 and 1.0 mm/year from the oldest to the youngest modeled earthquake during the episodic activity period of the fault (Figures 11 and 12). To calculate the long-term slip rate, about 4.4 m of slip is taken as having occurred in the time interval between the oldest and the youngest modeled rupture. This yields a likely long-term vertical slip rate of 0.7 mm/year during the period of ~2.2 to ~8 ka. The recurrence interval of approximately 2000 years was calculated for the activity period of the fault.

Simulations based on strip B database yield an earthquake at ca. 3.9 ka with colluvium level much higher than the upper part of this strip (see Appendix B), which correlates very well with the earthquake of ca. 3.7 ka in strip A. Running the code based on databases of strips C and D results in no simulation. The best fit to the ABCD database was a solution where only two earthquakes were derived, aged ca. 8.8 and 4.5 ka, but with high statistical goodness-of-fit criteria and scattered distributions (see Appendix B). However, the colluvium position before the reconstructed event at ca. 4.5 ka (ABCD database) and the earthquake of 3.7 ka old (A database) fit very well. The best-fit simulation based on the BCD database results in two earthquakes at 6.6 and 5.0 ka (see Appendix B), of which the older one has a slip that is much higher than the height of all the BCD strips, very close to the colluvium position of the earthquake of 6.0 ka old, based on the strip A database simulation.

4.1. Modeled past ruptures

The PDF of cosmogenic ^{36}Cl concentrations of strip A, which is the longest sampled strip, indicates more than one peak and shows the best fitting statistical criteria. Consequently, database A was used to analyze and model the rupture history (Figure 10). Without any modeling, at least three notable discontinuities are recognizable in strip A (Figure 9a), which reveals episodic activity of the fault through time.

Based on our modeling, the ground level was at the G_0 position before the occurrence of the first earthquake (Figure 13). Event 1, the oldest modeled earthquake, occurred ca. 8.1 ka ago with a slip value of about 3.4 m (S_1) (Figure 11). However, we consider this value as a minimum amount of slip, as the uppermost 1.2 m of the fault scarp was not suitable for sampling. The modeled colluvium position before this rupture was estimated to be about 40 cm higher than the top of the uppermost sample (G_0), at about 7.8 m up scarp (Figure 13), which moved to G_1 after the rupture (Figure 14a). To calculate the slip rate

Table 5. Mean chemical composition of the Priene–Sazlı samples and colluvium.

Sample name	Cl (%)	O (%)	C (%)	CaO (%)	MgO (%)	Al_2O_3 (%)	SiO_2 (%)	P_2O_5 (%)	K_2O (%)
PRI-A02	0.000966	50.83965	10.46729	51.50	2.46	0.57	1.41	0.02	0.14
PRI-A11	0.001121	48.98633	10.89106	53.80	1.41	0.63	1.57	0.01	0.16
PRI-A16	0.000444	50.65485	10.50966	55.40	0.57	0.56	1.37	0.02	0.14
PRI-A25	0.000667	50.74729	10.48847	52.00	2.54	0.83	1.75	0.02	0.19
PRI-A32	0.000697	47.04093	11.33603	55.20	0.60	0.60	1.41	0.01	0.14
PRI-A48	0.000792	51.11780	10.40372	51.60	0.74	1.61	3.37	0.02	0.33
PRI-A57	0.000365	52.13746	10.17064	50.10	4.38	1.13	2.60	0.02	0.24
PRI-A67	0.000609	58.25266	8.77217	42.70	9.33	0.51	1.62	0.02	0.13
PRI-B07	0.000555	45.37323	11.71743	53.60	0.44	0.18	0.43	0.01	0.04
PRI-B12	0.000464	47.41180	11.25127	51.80	1.02	0.37	0.82	0.01	0.08
PRI-C05	0.000907	54.26806	9.68329	44.10	5.94	0.74	2.14	0.01	0.18
PRI-C18	0.000599	47.22635	11.29365	54.10	0.89	0.41	1.01	0.01	0.09
PRI-D02	0.000956	50.93232	10.44610	50.30	1.32	0.31	4.86	0.01	0.08
PRI-D08	0.001981	51.57990	10.29777	48.60	4.66	0.58	1.13	0.01	0.17
Average	0.000660	50.11646	10.63273	51.05	2.59	0.65	1.82	0.01	0.15
	TiO_2 (%)	MnO (%)	Fe_2O_3 (%)	B (ppm)	Sm (ppm)	Gd (ppm)	U (ppm)	Th (ppm)	
PRI-A02	0.03	0.02	0.81	6.00	0.70	0.50	2.82	0.90	
PRI-A11	0.03	0.04	0.60	8.00	0.70	0.50	2.36	0.80	
PRI-A16	0.03	0.02	1.10	8.00	1.10	0.50	2.84	1.30	
PRI-A25	0.04	0.02	0.83	8.00	0.70	1.00	2.79	0.90	
PRI-A32	0.03	0.02	1.00	7.00	1.40	0.50	2.45	1.10	
PRI-A48	0.09	0.03	2.09	13.00	2.30	2.00	3.45	2.70	
PRI-A57	0.06	0.04	0.86	12.00	1.50	1.00	5.01	1.70	
PRI-A67	0.03	0.04	0.37	6.00	1.00	0.50	2.74	0.70	
PRI-B07	0.01	0.02	0.12	2.50	0.50	0.50	1.72	0.20	
PRI-B12	0.02	0.02	0.44	2.50	0.80	0.50	1.94	0.70	
PRI-C05	0.04	0.04	0.80	7.00	1.30	0.50	2.39	1.10	
PRI-C18	0.02	0.02	0.37	2.50	0.60	0.50	2.10	0.50	
PRI-D02	0.01	0.01	0.16	2.50	3.10	2.00	1.15	0.30	
PRI-D08	0.01	0.04	0.19	2.50	3.50	3.00	0.63	0.50	
Average	0.03	0.03	0.69	6.25	1.37	0.96	2.45	0.95	

until the time of the first modeled event, we considered the time interval between 21 ka and 8.1 ka. The calculated average slip rate is 0.3 mm/year, which we consider as a lower boundary, since the upper part of the scarp was not sampled; also, if there was an earthquake before the first modeled rupture, it would be younger than 21 ka, which would result in a higher slip rate.

Event 2, the second rupture, was identified at a height of ca. 4.4 m on the fault scarp, 2.2 ka after the first event (Figure 11). Thus, the fault experienced a rupture ca. 6.0 ka ago with a slip of ca. 1.5 m (S_2). The ground level shifted from G_1 to G_2 (Figure 14b). However, the main discontinuity is identified in the PDF plot at a height of about 5.5 m, which is higher than the height of the modeled event (Figure 10a). This difference is explained by the approximate nature of the PDF approach, which can be used for initial points of simulation (Figure 10a). A slip of ca. 1.5 m over the time span between the first and second ruptures results in a mean slip rate of ca. 0.7 mm/year.

Before the occurrence of Event 3, the fault remained quiet for ca. 2.2 ka. The subsequent earthquake struck ca. 3.7 ka ago (Figure 11), causing a fault rupture with ca. 1.4

Table 6. Parameters of the sampled fault scarp.

Latitude Longitude Altitude	37°38.895′N 27°15.421′E 52 m			
	Strip A	Strip B	Strip C	Strip D
Scarp strike	N66°E	N45°E	N68°E	N60°E
Scarp dip	52°	55°	52°	50°
Colluvium dip Scarp height Top surface dip	20° 8.5 m 31°			
Rock density Colluvium density Rock water content Colluvium water content	2.4 g/cm^3 1.5 g/cm^3 0.2% 1%			

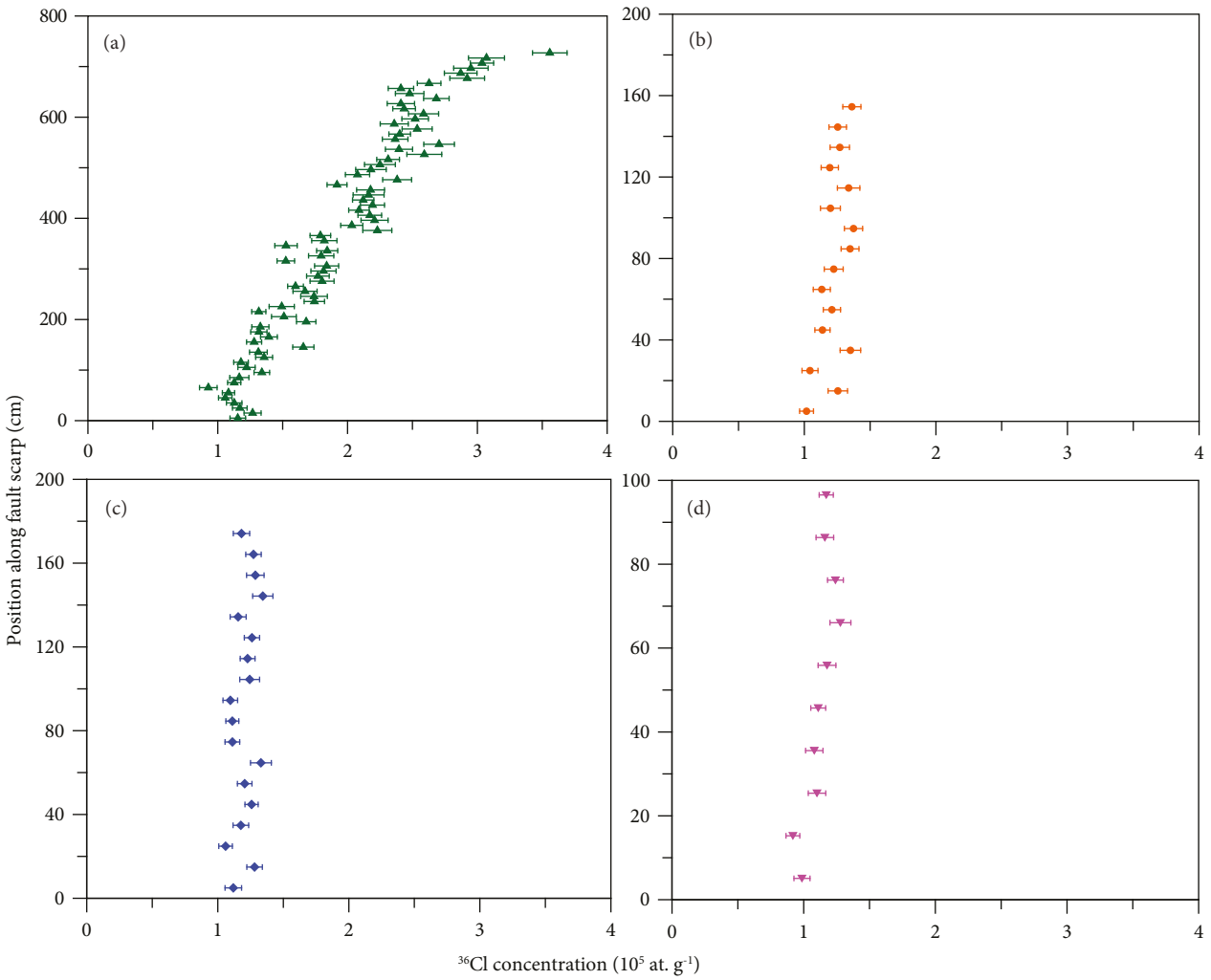

Figure 9. Cosmogenic ^{36}Cl concentrations with 1σ uncertainties versus height along (a) strip A, (b) strip B, (c) strip C, and (d) strip D.

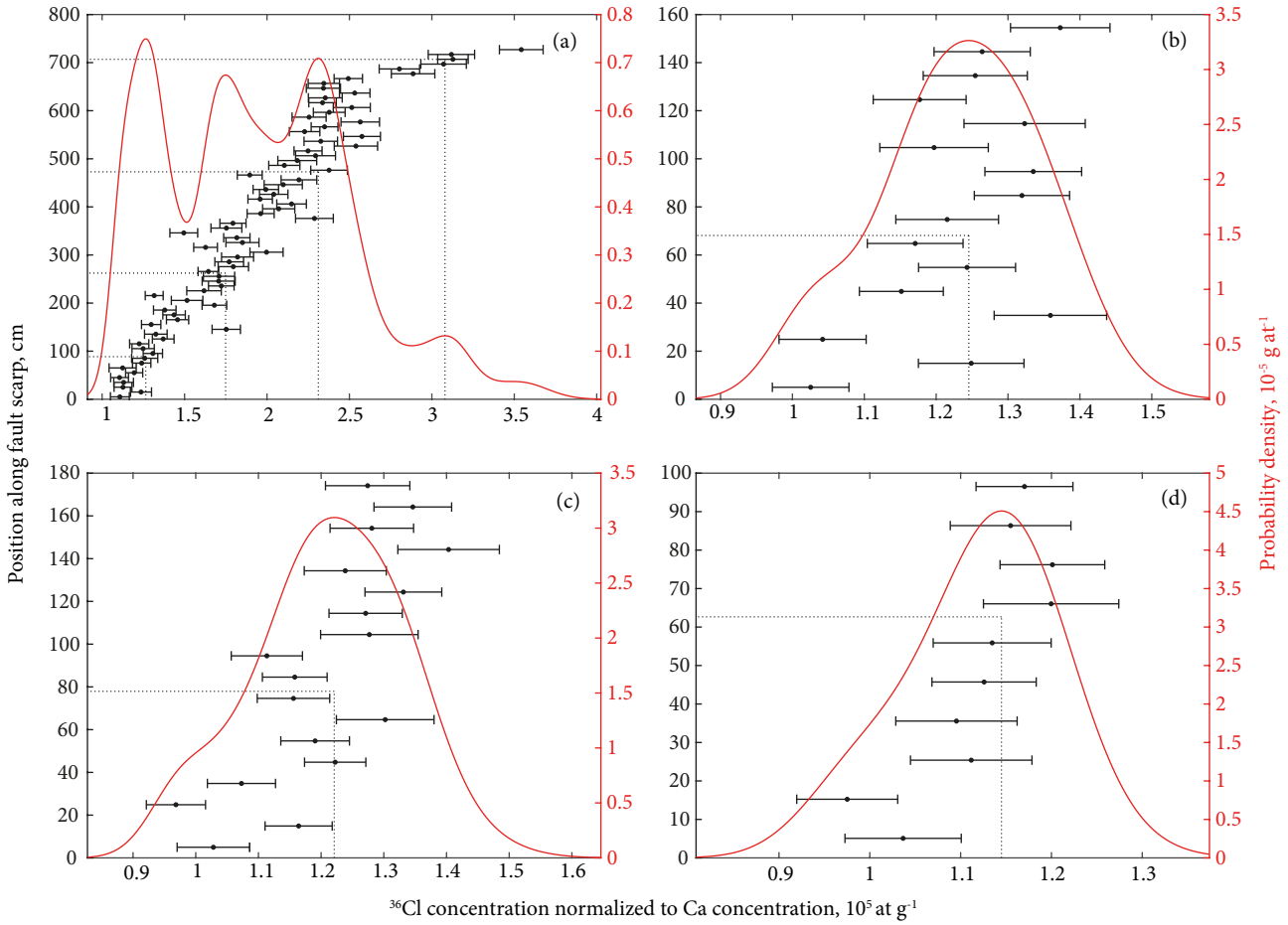

Figure 10. The PDF (probability density function) plot of ^{36}Cl concentrations normalized to Ca concentrations of (a) strip A, (b) strip B, (c) strip C, and (d) strip D.

m of slip (S_3) and a movement in the ground level to G_3 (Figure 14c). This discontinuity at a height of about 2.8 m fits very well with the second peak of the PDF plot with about 40 cm of difference in height (Figure 10a). An average slip rate of about 0.6 mm/year was obtained by taking into account the related quiescence phase since the occurrence of the previous rupture before this event.

Event 4, the last modeled earthquake, occurred 2.2 ka ago, after 1.5 ka of inactivity, with 1.5 m of slip (S_4) (Fig. 11), which caused ground level displacement to the modern level (G) (Figure 14d). This event has a perfect match with the discontinuity shown in the PDF graph (Figure 10a). The mean slip value of 1.0 mm/year was calculated for the time span between the third and final modeled earthquakes. This event correlates well with the destructive historical earthquake of 68 CE, which had an intensity of VII (Ergin et al., 1967).

We included the earthquake of July 1955 as input for our seismic scenarios, but could not yield a better fit to resolve it in our databases. In the best-fit solutions of five- and six-event scenarios based on database A, the slip amounts of the youngest modeled earthquake were either zero or very small (Table 7). Furthermore, modeling of the strip B database results in an earthquake at time zero, but with no displacement, which is not plausible. For a fault with a length of at least 30 km, a much higher amount of slip is expected than a few decimeters (see Section 5.2 and Table 8). One possibility is that the section of the fault segment that we analyzed in this study was not ruptured by the earthquake (after Emre et al., 2016). However, this hypothesis seems to be unlikely because the observed surface rupture is present along almost the entire length of the fault, as indicated by Şaroğlu et al. (1992). Another explanation could be that the surface of this rupture along strip A, which is supposed to have been exposed by the last earthquake, could still be under colluvium. Hence, the lower part of strip A was covered by collapsed colluvium from the top surface after the 1955 CE rupture. In this case, reconstruction of this earthquake would only have been possible if the fault scarp under the colluvium had been

Table 7. Output results for the data set from strip A of the Priene–Sazli fault scarp along with statistical criteria.

Database	Event number	Beginning of exposure (ka)	Age (ka)	Slip (m)	Statistical criteria
A	4	21	8.1 6.0 3.7 2.2	3.4 1.5 1.4 1.5	$\chi^2 = 2.9$ RMSw = 1.6 AICc = 291
A	5	22	7.3 5.8 3.7 2.1 0.07	4.0 1.1 1.4 1.7 0.0	$\chi^2 = 3.0$ RMSw = 1.6 AICc = 297
A	6	19	7.9 5.6 3.6 2.3 0.1 0.01	3.6 1.8 1.1 1.4 0.1 0.0	$\chi^2 = 3.1$ RMSw = 1.6 AICc = 301
B	2	15	3.9 0.0	4.7 0.0	$\chi^2 = 2.4$ RMSw = 1.2 AICc = 97
BCD	2	7	6.6 5.0	8.2 1.5	$\chi^2 = 3.0$ RMSw = 1.6 AICc = 215
ABCD	2	18	8.8 4.5	3.2 8.4	$\chi^2 = 3.4$ RMSw = 1.7 AICc = 454

Chi-squared value: χ^2.
Weighted root mean square: RMSw.
Akaike information criterion: AICc.

sampled and analyzed. We do not exclude the potential of collapse of colluvium on the base of the fault scarp as a consequence of successive ruptures; however, based on field evidence this hypothesis seems to be unlikely. The most probable explanation is that an exposure age of less than 100 years is too short to let variable accumulation of ^{36}Cl on the fault scarp be differentiated as a discontinuity on the ^{36}Cl profile.

The recurrence interval of destructive earthquakes is highly dependent on the dynamic behavior of a given fault, which is an essential factor in conducting earthquake risk assessment. According to our results, the inactivity periods between successive events on the fault are between 1.5 and 2.2 ka. Thus, we can deduce that the major earthquakes on the Priene–Sazlı Fault repeat in a roughly similar seismic cycle of ca. 2000 years. This interval is also consistent with the occurrence of the earthquake of 1955 CE, even though this event was not detected by the modeling code in this section of the fault.

5. Discussion

Consideration of the seismic history of major faults is a key issue in order to estimate the approximate timing and size of their probable activity and minimize damage (e.g., Scholz, 2002). We determined the time-slip history of the Priene–Sazlı Fault Zone in the BMG system, which is one of the major structures in the seismically active Western Anatolian Extensional Province. The existing historical and instrumental seismic data from this fault indicate that the 68 CE and 1955 CE earthquakes and accompanying surface ruptures were generated along this fault in the past 2000 years. Our analysis reveals four major events including the 68 CE event, which indicates that the Priene–Sazlı Fault is an active fault that was displaced with cumulative vertical displacement of at least 7.8 m during the Holocene (Figure 11). It should be mentioned that the number of modeled earthquakes is the minimum, since the code is unable to identify small ruptures, which were not able to displace the fault (cf. Schlagenhauf et al., 2010). The time

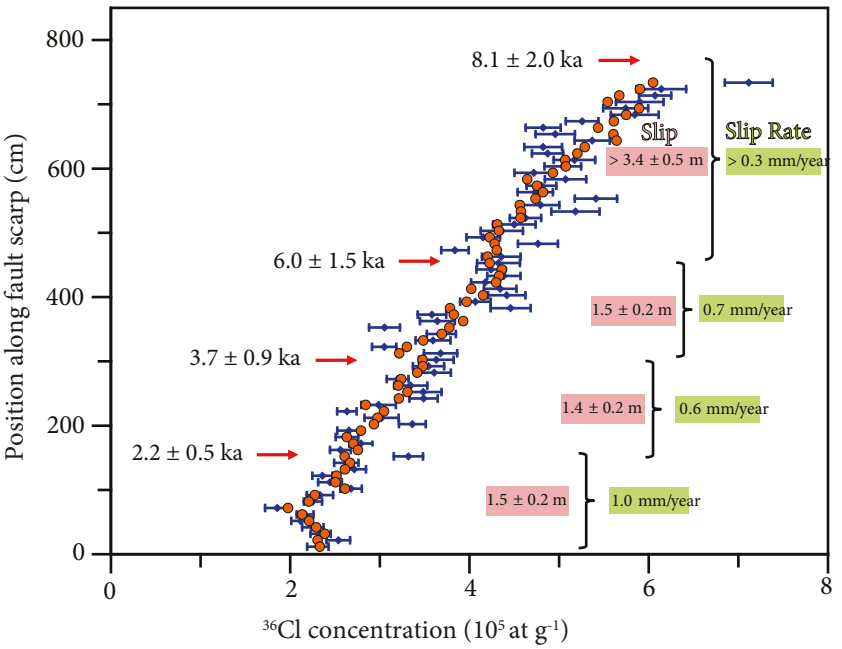

Figure 11. Best fit (orange circles) of strip A of the Priene–Sazlı Fault scarp data with a four-rupture model. Blue dots are measured ^{36}Cl concentrations with 1σ uncertainties. Red arrows mark the colluvium positions before the modeled ruptures. Slip rates are calculated individually for each earthquake, based on the slip value and the time period between two successive earthquakes.

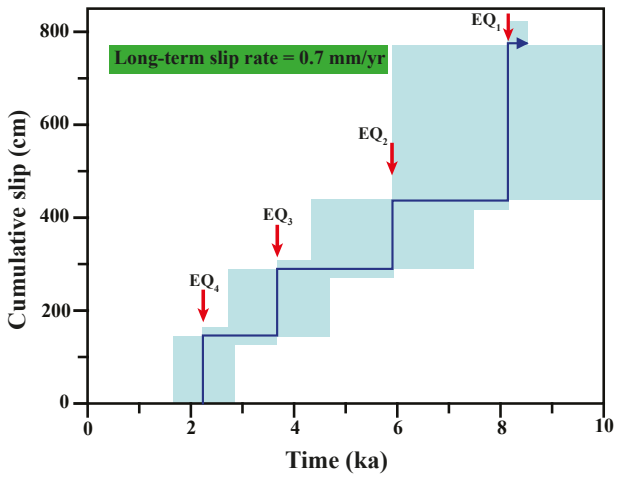

Figure 12. Time versus cumulative slip amount along with uncertainties of time and colluvium position before earthquakes obtained from modeling of the Priene–Sazlı Fault scarp. The average slip rate is 0.7 mm/year.

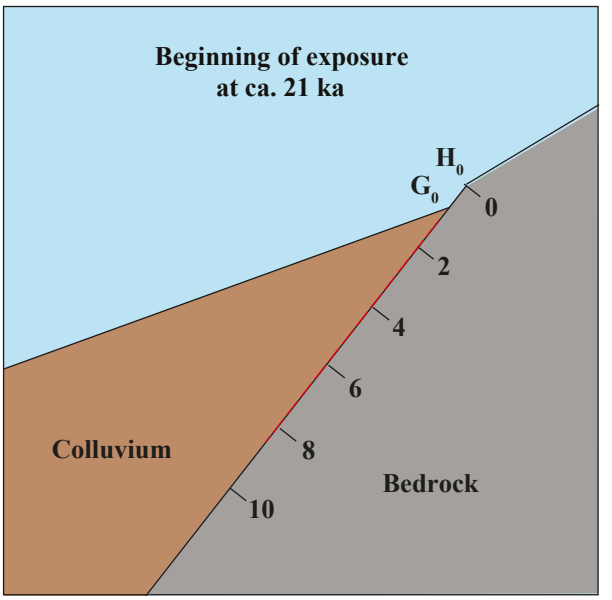

Figure 13. Schematic sketch of the Priene–Sazlı Fault scarp before its active period. Red dashed line shows the sampled surface. The fault surface grade is in meters. H_0 and G_0 show scarp height and ground level prior to the first rupture. Note that 1.2 m of the uppermost part of the fault scarp was not sampled.

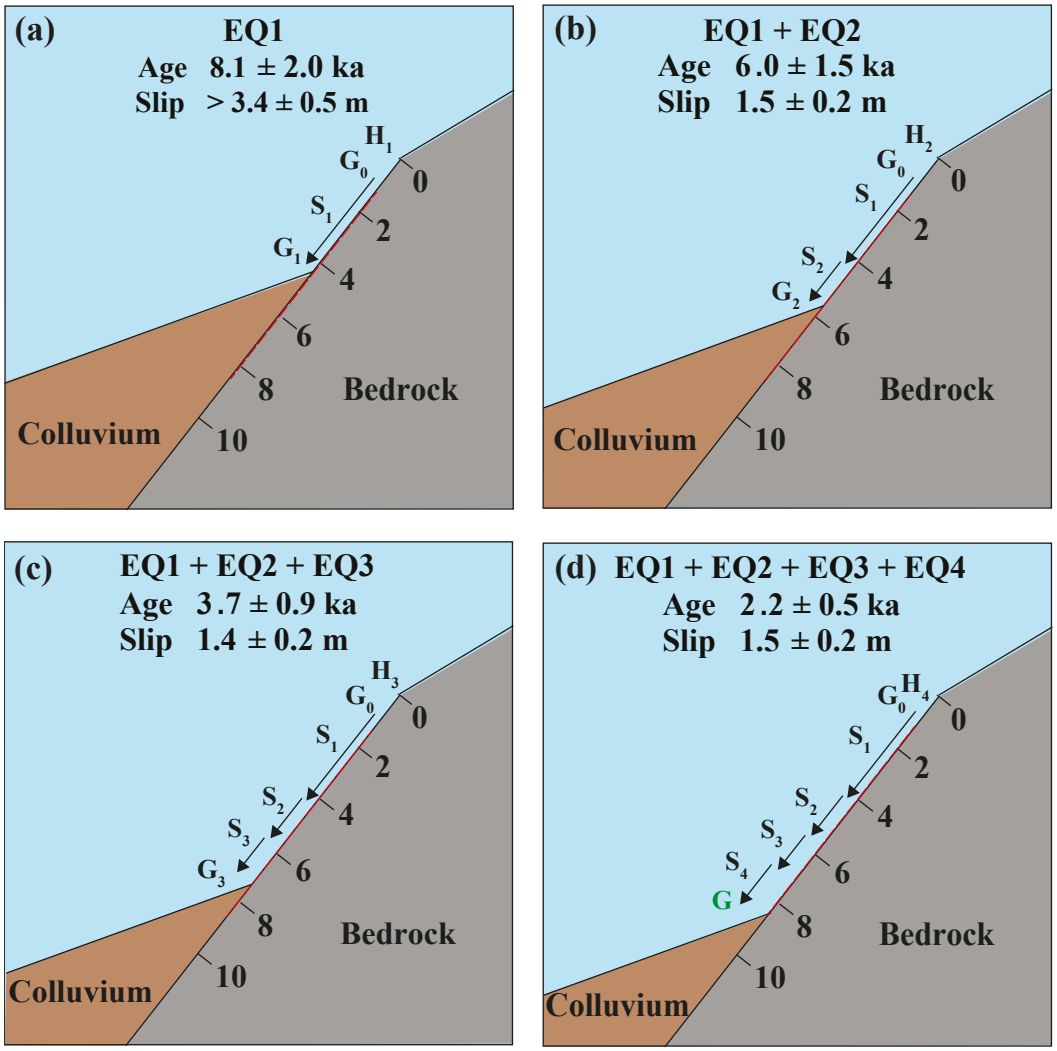

Figure 14. Schematic sketch of the Priene–Sazlı Fault scarp showing colluvium position and episodic fault exposure during four modeled earthquake events. Red dashed line shows the sampled surface. The fault surface grade is in meters. H_1 to H_4 (height of the fault scarp) following earthquakes 1 to 4, respectively; G_0 (ground level just before the first rupture), G_1 to G_3 are ground level before the second, third, and fourth ruptures, and G is the current ground level. S_1 to S_4 represent the slip amounts of the four earthquakes related to the past to recent events.

and slip precision are influenced by many factors and can be stated to be about 25% (2σ) and 15% (2σ), respectively. This amount is estimated based on measurement errors of AMS, parent elements, production rates, rock density, and approximation of scarp geometry, including chipped sample faces. Differentiation of earthquakes clustered close in time, within the uncertainties for the age and slip, is not possible if the discontinuity in the ^{36}Cl profile is not prominent (Tikhomirov, 2014). Accordingly, the calculated slip value is the upper bound. The recurrence interval of the paleoearthquakes is obtained by taking into account the time of the ruptures. The vertical slip rate for each earthquake is calculated based on the amount of slip.

5.1. Magnitude of future ruptures

Definitive prediction of future earthquake magnitudes is not possible by any of the available seismological methods. However, the potential maximum magnitudes of earthquakes can be estimated by empirical relationships as a logarithmic factor of the fault surface rupture length in order to assess an earthquake hazard (e.g., Wells and Coppersmith, 1994; Ambraseys and Jackson, 1998; Pavlides and Caputo, 2004). First, we refer to the study conducted by Pavlides and Caputo (2004), who specifically focused on dip-slip normal faults in the Aegean region, including Western Anatolia and the Priene–Sazlı Fault (Table 8, Eq. (1)). Taking into account the 35-km surface

Table 8. Regression of SRL (surface rupture length), Magnitude (Ms/M), and vertical displacement (MVD/MD) calculated for the Priene–Sazli Fault. The units of slip, MVD, and MD are meters. MVD (maximum vertical displacement) is converted to slip or MD (maximum displacement) by applying fault surface dip (Sin (θ) = vertical displacement/slip).

	Sin (θ) = vertical displacement / slip θ = 52°	SRL = 35 km (Şaroğlu et al., 1992)
Pavlides and Caputo (2004)	Ms = 0.9 × log (SRL) + 5.48 (Eq. (1))	6.9
	Log (MVD) = 1.14 × Ms – 7.82 (Eq. (2))	MVD = 1.1 Slip = 1.4
Wells and Coppersmith (1994)	M = 4.86 + 1.32 × log (SRL) (Eq. (3))	6.9
	Log (MD) = –5.90 + 0.89 × M (Eq. (4))	MD (slip) = 1.7

rupture length for the Priene–Sazlı Fault (Şaroğlu et al., 1992), an earthquake with magnitude of 6.9 is expected if the fault is activated. Secondly, we consider the equation of Wells and Coppersmith (1994), which was compiled based on diverse normal faults worldwide (Table 8, Eq. (3)); the probable magnitude is similar (Table 8). Whichever method is used, the Priene–Sazlı Fault is classified as a seismogenic fault, which is characterized by having the potential to produce earthquakes with values larger than magnitude 5 (McCalpin, 2009).

5.2. Magnitude of the modeled events and plausibility of modeling

We used empirical relationships that connect the displacement value with the corresponding earthquake magnitude in our modeling. According to the relationship of Pavlides and Caputo (2004), which relates maximum vertical displacement (MVD) value to magnitude (Ms) (Table 8, Eq. (2)), the MVD is expected to be 1.1 m, which equates to 1.4 m of slip, for an earthquake of magnitude 6.9. Since only the slip value (=MD) is determined in our modeling, we convert it to MVD by accounting for a dip of θ = 52° for the fault scarp surface along strip A (Figure 1b; Tables 8 and 9). In addition, based on Wells and Coppersmith (1994) (Table 8, Eq. (4)), the maximum displacement (MD) resulting from an earthquake with a magnitude of 6.9 is 1.7 m. The magnitude values of the modeled earthquakes were calculated using the relationships of Pavlides and Caputo (2004) (Table 9, Eq. (5)) and Wells and Coppersmith (1994) (Table 9, Eq. (6)). Calculation of magnitudes by taking uncertainties of modeled slip into account caused negligible variation in the final value or similar values in some cases. Therefore, we ignored the uncertainties of magnitude to avoid any complexity.

Event 1, the oldest movement, has a vertical displacement of 2.7 ± 0.4 m and an average modeled slip of 3.4 ± 0.5 m. Based on either Eq. (5) or (6), an earthquake with magnitude of at least 7 is required to produce such a large amount of displacement. Thus, we assume that the fault experienced a cluster of smaller ruptures in a short period of time that produced the displacement, rather than an individual earthquake. The FSDT code recognizes earthquakes that occur within a short time interval as a single event. However, minor discontinuities are recognizable between the main curves, which indicate smaller earthquakes that are not differentiated by the code within the uncertainties of the study (Figure 11). In addition, taking into account either Eq. (2) or (4), the fault needs to experience at least two or three ruptures of 6.9 to expose about 3.4 m at once. Thus, this modeled rupture is interpreted as several smaller subevents rather than a unique event. Event 2, the second modeled rupture with 1.5 ± 0.2 m of slip, equates to 1.2 ± 0.2 m of the MVD, which was likely produced by an earthquake of magnitude 6.7–6.8, according to Eqs. (5) and (6). Based on Eqs. (2) and (4), one or two earthquake(s) is/are responsible for producing this amount of slip. Event 3, the third modeled earthquake, caused a fault rupture of 1.4 ± 0.2 m of slip, which equates to 1.1 ± 0.2 m of the MVD. An earthquake with magnitude 6.7–6.8 is able to generate this amount of slip based on Eqs. (5) and (6). Taking into account Eqs. (2) and (4), one earthquake is required to expose this amount of slip on the fault. Event 4, the last modeled earthquake with an equal amount of slip to Event 4, is interpreted as having been produced by one or two earthquake(s).

5.3. Regional comparison

Putting our results into a regional context, the recurrence interval of earthquakes and the slip rates for the Priene–

Table 9. Regression of magnitude (MS/M) and vertical displacement (MVD/MD) for the Priene–Sazli Fault. *Modeled by the code. MVD (maximum vertical displacement) is converted to slip or MD (maximum displacement) by applying fault surface dip (Sin (θ) = vertical displacement/slip).

Sin (θ) = vertical displacement / slip θ = 52°		Event	Slip* (m)	MVD (m)	Ms
Pavlides and Caputo (2004)	Ms = 0.59 × log (MVD) + 6.75 (Eq. (5))		Lowest χ^2	Average	Average
		1	3.4 ± 0.5	2.7 ± 0.4	7.0
		2	1.5 ± 0.2	1.2 ± 0.2	6.8
		3	1.4 ± 0.2	1.1 ± 0.2	6.8
		4	1.5 ± 0.2	1.2 ± 0.2	6.8
		Event	MD (=slip*) (m)	M	
Wells and Coppersmith (1994)	M = 6.61 + 0.71 × log (MD) (Eq. (6))		Lowest χ^2	Average	
		1	3.4 ± 0.5	7.0	
		2	1.5 ± 0.2	6.7	
		3	1.4 ± 0.2	6.7	
		4	1.5 ± 0.2	6.7	

Sazlı Fault are compatible with previous studies in Western Anatolia. For example, the Havran–Balıkesir and Edremit fault zones in the northern part of Western Anatolia with recurrence interval of earthquakes in the range of 1000–2000 years were documented by Sözbilir et al. (2016a, 2016b). In addition, our results fit the upper limit of the recurrence interval for major earthquakes in the Büyük Menderes Fault Zone of 250–1900 years (Altunel et al., 2009). The short-term calculated slip rate is also in accordance with slip rates yielded over longer time intervals on several normal faults along the strike of the Gediz Graben (Figure 2). Kent et al. (2017) reported average vertical slip rates of 0.7, 1.0, and 1.2 mm/year, respectively, for the Turgutlu, Alaşehir, and Salihli fault segments over the last 2.6 Ma. Furthermore, the minimum calculated slip rate in our study is compatible with the upper limit for the vertical slip rate of at least 0.3 mm/year during the Plio-Pleistocene for the Manastır Fault in the Gediz Graben (Özkaymak et al., 2011). Emre et al. (2016) estimated the maximum magnitude of a potential earthquake on the Söke (Priene–Sazlı) Fault to be about 6.3 to 6.6, based on the empirical relationship of Wells and Coppersmith (1994). The reason why they obtained smaller magnitudes is that they considered the fault to be made up of two segments, 13 and 22 km long.

6. Conclusions

In this study, we tracked the occurrence of paleoearthquakes prior to the known historical earthquakes in the Priene–Sazlı Fault Zone in the BMG system in Western Anatolia, which is one of the seismically most active regions of the world. In order to deduce the long-term sequence of associated paleoearthquakes, we analyzed cosmogenic ^{36}Cl in 117 samples taken along the well-exposed fault surface. We modeled past ruptures and reconstructed their chronology with the Fault Surface Dating Tool (Tikhomirov, 2014). Using the modeling results, we determined the average slip rates, the recurrence intervals for destructive earthquakes, and the magnitude of expected future earthquakes.

Our results indicate that the Priene–Sazlı fault experienced at least four large seismic events during the Holocene at 8.1 ± 2.0, 6.0 ± 1.5, 3.7 ± 0.9, and 2.2 ± 0.5 ka, with vertical slips of 1.4 ± 0.2 to 3.4 ± 0.5 m, the maximum displacement being associated with the oldest event. However, closer analysis implies that the oldest event is likely to be a series of earthquakes that occurred within a short time span. The average earthquake recurrence interval of ca. 2000 years was calculated for the Priene–Sazlı Fault. Mean vertical slip rates greater than 0.3, 0.7, 0.6, and 1.0 mm/year were calculated from the oldest to the youngest rupture. An average long-term slip rate of 0.7 mm/year was estimated for this fault. The analysis of the seismic behavior of the Priene–Sazlı Fault showed that this fault produces series of earthquakes within a short time interval during periods of high seismic activity.

Cosmogenic ^{36}Cl fault scarp dating is a powerful tool, with which the history and slip rate of an active fault plane can be determined directly. Therefore, it has great potential to improve our knowledge for better seismic risk assessment in highly urbanized regions such as Western Anatolia, where major normal faults in carbonate bedrock dominate. Furthermore, the

earthquakes of 1955 CE and 68 CE (2.2 ka earthquake in our modeling), as well as our earthquakes modeled at ca. 8.1, 6.0, and 3.7 ka, illustrate the high seismic activity of the fault during the Holocene. Based on the interval between the large events, the occurrence of the next high seismicity period of the fault in 2000 years is not beyond expectation. Acceleration of slip rates in large-scale fault zones, similar to the values for the Priene–Sazlı Fault, can imply more activity on the fault through time in terms of higher magnitude and/or frequency of earthquakes. According to the calculated long-term slip rate, slip per event, rupture length, magnitude of possible earthquakes, and recurrence interval of the Priene–Sazlı Fault, we classify this fault as a low to moderately (class 3) active fault according to the classification of Cluff and Cluff (1984) for earthquake engineering.

Acknowledgments

We are grateful to Prof Dr Hans-Arno Synal and the team at the Laboratory of Ion Beam Physics, ETH Zurich, for their support with the AMS measurements. We wish to thank Dr Çağlar Özkaymak for his collaboration with sample preparation. We would also like to thank the students and technicians of Dokuz Eylül University, who helped us during our sampling campaign. The quality of the paper has benefited from constructive reviews by Dr Taylan Sançar and the three anonymous reviewers, who are especially acknowledged. This study was jointly funded by Dokuz Eylül University (Research Project No. 2007. KB.FEN.047), the Surface Exposure Dating Laboratory at the University of Bern, the Bern University Research Foundation, and the Swiss National Science Foundation (Project No. 200021-147065).

References

Akçar N, Tikhomirov D, Özkaymak Ç, Ivy-Ochs S, Alfimov V et al. (2012). ^{36}Cl exposure dating of paleoearthquakes in the Eastern Mediterranean: first results from Western Anatolian Extensional Province, Turkey. GSA Bulletin 124 (11/12): 1724-1735.

Aktug B, Nocquet JM, Cingoz A, Parsons B, Erkan Y et al. (2009). Deformation of western Turkey from a combination of permanent and campaign GPS data: limits to block-like behavior. Journal of Geophysical Research 114 (B10): B10404.

Alfimov V, Ivy-Ochs S (2009). How well do we understand production of Cl-36 in limestone and dolomite?. Quaternary Geochronology 4 (6): 462-474.

Altunel E (1998) Evidence for damaging historical earthquakes at Priene, Western Turkey. Turkish Journal of Earth Sciences 7: 25-35.

Altunel E, Akyüz S, Meghraoui M, Kiyak Nafiye G, Karabacak V et al (2009). *Büyük Menderes Fay Zonunun Arkeosismolojisi* ve *Paleosismolojisi. TÜBİTAK Research Project No. 105Y348. Final Report. Ankara, Turkey: TÜBİTAK (in Turkish).*

Ambraseys N (2009). Earthquakes in the Mediterranean and Middle East: A Multidisciplinary Study of Seismicity up to 1900. Cambridge, UK: Cambridge University Press.

Ambraseys N, Jackson JA (1998). Faulting associated with historical and recent earthquakes in the Eastern Mediterranean region. Geophysical Journal International 133 (2): 390-406.

Ambraseys NN (1971). Value of historical records of earthquakes. Nature 232: 375-379.

Ambraseys NN (1975). Studies in Historical Seismicity and Tectonics. Geodynamics Today, Chapter 2. London, UK: The Royal Society.

Angelier J, Dumont JF, Karamanderesi İH, Poission A, Şimşek Ş et al. (1981). Analyses of fault mechanisms and expansion of southwestern Anatolia since the Late Miocene. Tectonophysics 75: 11-19.

Barnett JAM, Mortimer J, Rippon JH, Walsh JJ, Watterson J (1987). Displacement geometry in the volume containing a single normal fault. American Association of Petroleum Geologists Bulletin 71: 925-937.

Beck J, Wolfers S, Roberts JP, 2018. Bayesian earthquake dating and seismic hazard assessment using chlorine-36 measurements (BED v1). Geoscientific Model Development 11: 4383–4397.

Benedetti L, Finkel R, King G, Armijo R, Papanastassiou D et al. (2003). Motion on the Kaparelli fault (Greece) prior to the 1981 earthquake sequence determined from Cl-36 cosmogenic dating. Terra Nova 15 (2): 118-124.

Benedetti L, Finkel R, Papanastassiou D, King G, Armijo R et al. (2002). Post-glacial slip history of the Sparta fault (Greece) determined by Cl-36 cosmogenic dating: evidence for non-periodic earthquakes. Geophysical Research Letters 29 (8): 1246.

Benedetti L, Manighetti I, Gaudemer Y, Finkel R, Malavieille Y et al. (2013). Earthquake synchrony and clustering on Fucino faults (Central Italy) as revealed from in situ ^{36}Cl exposure dating. Journal of Geophysical Research: Solid Earth 118: 4948-4974.

Bozkurt E (2000). Timing of extension on the Büyük Menderes Graben, Western Turkey, and its tectonic implications. In: Bozkurt E, Winchester JA, Piper JDA (editors). Tectonics and Magmatism in Turkey and the Surrounding Area, Special Publications Vol. 173. London, UK: Geological Society, pp. 385-403.

Broughton TRS (1938). An Economic Survey of Ancient Roma. Vol. IV. Baltimore, MD, USA: Johns Hopkins Press.

Bubeck A, Wilkinson M, Roberts GP, Cowie PA, McCaffrey KJW et al. (2015). The tectonic geomorphology of bedrock scarps on active normal faults in the Italian Apennines mapped using combined ground penetrating radar and terrestrial laser scanning. Geomorphology 237: 38-51.

Calvi VS (1941). Erdbebenkatalog der Turkei und Einiger Benaehbarter Gabiete. Yayınlanmış, Rapor No. 276. Ankara, Turkey: MTA (in Turkish).

Canıtez N, Üçer SB (1967). Computer determinations for the fault plane solutions in and near Anatolia. Tectonophysics 4 (3): 235-244.

Caputo R, Pavlides S, Papadopoulos G, Helly B (1998). Palaeoseismological researches in northern Thessaly, Greece. In: Preliminary Results: XXVI. General Assembly of the ESC, Abstracts, Tel Aviv, Israel, p. 25.

Christl M, Vockenhuber C, Kubik PW, Wacker L, Lachner J et al. (2013). The ETH Zurich AMS facilities: performance parameters and reference materials. Nuclear Instruments and Methods in Physics Research B 294: 29-38.

Çifçi G, Pamukçu O, Çoruh C, Çopur S, Sözbilir H (2011). Shallow and deep structure of a supradetachment basin based on geological, conventional deep seismic reflection sections and gravity data in the Buyuk Menderes Graben, Western Anatolia. Surveys in Geophysics 32 (3): 271-290.

Çiftçi NB, Bozkurt E (2009). Evolution of the Miocene sedimentary fill of the Gediz Graben, SW Turkey. Sedimentary Geology 216: 49-79.

Cluff LS, Cluff JL (1984). Importance of assessing degrees of fault activity for engineering decisions. In: Proceedings of the 8th World Conference on Earthquake Engineering, pp. 629-636.

Collection Academique (1766). Tome VI de la Partie Entrange et Premier Tome de la Physique Experimentale Separee. Paris, France: Collection Academique (in French).

Cowie PA, Phillips RJ, Roberts GP, McCaffrey K, Zijerveld LJJ et al. (2017). Orogen-scale uplift in the central Italian Apennines drives episodic behaviour of earthquake faults. Scientific Reports 7: 44858.

Desilets D, Zreda M, Almasi PF, Elmore D (2006). Determination of cosmogenic Cl-36 in rocks by isotope dilution: Innovations, validation and error propagation. Chemical Geology 233 (3-4): 185-195.

Dewey JF, Şengör AMC (1979). Aegean and surrounding region: complex multiplate and continuum tectonics in a convergent zone. Geological Society of America Bulletin 90: 84-92.

Dikmen G (1952). Nazilli, Tarih ve Cografyası. Aydın, Turkey: Aydın İl Halk Kütüphanesi (In Turkish).

Duman TY, Çan T, Emre Ö, Kadirioğlu FT, Başarır Baştürk N et al. (2016). Seismotectonics database of Turkey. Bulletin of Earthquake Engineering 16 (8): 3277-3316.

Duman TY, Emre Ö, Özalp S, Elması H (2011). Active Fault Map Series of Turkey (scale 1:250,000) Aydın (NJ 35-11). Ankara, Turkey: MTA.

Dumont JF, Uysal Ş, Şimşek Ş, Karamanderesi İH, Letouzey J (1979). Formation of the grabens in southwestern Anatolia. General Directorate of Mineral Research and Exploration Bulletin 92: 7-18.

DuRoss CH, Personius SF, Crone AJ, Olig SS, Hylland MD et al. (2016). Fault segmentation: new concepts from the Wasatch Fault Zone, Utah, USA. Journal of Geophysical Research: Solid Earth 121: 1131-1157.

Elmore D, Ma X, Miller T, Mueller K, Perry M et al. (1997). Status and plans for the PRIME Lab AMS facility. Nuclear Instruments and Methods in Physics Research Section B 123 (1-4): 69-72.

Emre Ö, Duman TY, Özalp S, Elması H, Olgun Ş et al. (2013). Active Fault Map of Turkey (Scale 1:250,000), General Directorate of Mineral Research and Exploration Special Publication Series 30. Ankara, Turkey: MTA.

Emre Ö, Duman TY, Özalp S, Şaroğlu F, Olgun Ş et al. (2016). Active fault database of Turkey. Bulletin of Earthquake Engineering 16 (8): 3229-3275.

Emre T, Sözbilir H (1997). Field evidence for metamorphic core complex, detachment faulting and accommodation faults in the Gediz and Büyük Menderes grabens, western Anatolia. In: Pişkin Ö, Ergün M, Savaşcın MY, Tarcan G (editors). Proceedings of International Earth Sciences Colloquium on the Aegean Region, Vol. 2, pp. 73-93.

Ergin K, Güçlü U, Uz Z (1967). A Catalog of Earthquake for Turkey and Surrounding Area (11 A.D. to 1964 A.D.). İstanbul, Turkey: İTU Faculty of Mining Engineering.

Evans JM, Stone JOH, Fifield LK, Cresswell RG (1997). Cosmogenic chlorine-36 production in K-feldspar. Nuclear Instruments and Methods in Physics Research Section B 123 (1-4): 334-340.

Eyidoğan H (1988). Rates of crustal deformation in western Turkey as deduced from major earthquakes. Tectonophysics 148: 83-92.

Fink D, Vogt S, Hotchkis M (2000). Cross-sections for Cl-36 from Ti at E-p=35-150 MeV: applications to in-situ exposure dating. Nuclear Instruments and Methods in Physics Research Section B 172: 861-866.

Guidoboni E, Comastri A, Traina G (1994). Catalogue of Ancient Earthquakes in the Mediterranean Area up to 10th Century. Bologna, Italy: Istituto Nazionale di Geofisica.

Gürer ÖF, Bozcu M, Yılmaz K, Yılmaz Y (2001). Neogene basin development around Söke-Kuşadası (western Anatolia) and its bearing on tectonic development of the Aegean region. Geodinamica Acta 14: 57-69.

Gürer ÖF, Sarica-Filoreau N, Özburan M, Sangu E, Doğan B (2009). *Progressive development* of the *Büyük Menderes Graben* based on new data, western Turkey. Geological Magazine 146: 652-673.

Hancock PL, Barka AA (1987). Kinematic indicators on active faults in western Turkey. Journal of Structural Geology 9 (5/6): 573-584.

Harrington CD, Whitney JW, Jull AJT, Phillips W (2000). Cosmogenic dating and analysis of scarps along the Solitario Canyon and Windy Wash Faults, Yucca Mountain, Nevada. In: Whitney JW, Keefer WR (editors). Geologic and Geophysical Characterization Studies of Yucca Mountain, Nevada, A Potential High-Level Radioactive-Waste Repository. Washington, DC, USA: US Geological Survey Digital Data Series.

Heisinger B, Lal D, Jull AJT, Kubik P, Ivy-Ochs S et al. (2002a). Production of selected cosmogenic radionuclides by muons: 1. Fast muons. Earth and Planetary Science Letters 200 (3-4): 345-355.

Heisinger B, Lal D, Jull AJT, Kubik P, Ivy-Ochs S et al. (2002b). Production of selected cosmogenic radionuclides by muons: 2. Capture of negative muons. Earth and Planetary Science Letters 200 (3-4): 357-369.

Ivy-Ochs S, Poschinger AV, Synal HA, Maisch M (2009). Surface exposure dating of the Flims landslide, Graubunden, Switzerland. Geomorphology 103 (1): 104-112.

Ivy-Ochs S, Synal HA, Roth C, Schaller M (2004). Initial results from isotope dilution for Cl and Cl-36 measurements at the PSI/ETH Zurich AMS facility. Nuclear Instruments and Methods in Physics Research Section B 223-24: 623-627.

Jackson JA, McKenzie D (1988). Rates of active deformation in the Aegean Sea and 669 surrounding areas. Basin Research 1: 121-128.

Kadirioğlu FT, Kartal RF, Kılıç T, Kalafat D, Duman TY et al. (2018). An improved earthquake catalogue (M ≥ 4.0) for Turkey and its near vicinity. Bulletin of Earthquake Engineering 16 (8): 3317–3338.

Kalafat D (1998). Anadolu'nun tektonik yapılarının deprem mekanizmaları açısından irdelenmesi. Deprem Araştırma Bülteni 77: 1-217 (In Turkish).

Kalafat D, Kekovalı K, Güneş Y, Yılmazer M, Kara M et al. (2009). Türkiye ve Çevresi Faylanma-Kaynak Parametreleri (MT) Kataloğu (1938–2008). Istanbul, Turkey: Boğaziçi University (in Turkish).

Karnik V (1971). Seismicity of the European Area 2.D. Dordrecht, the Netherlands: Reidel Publishing Company.

Kent E, Boulton SJ, Stewart IS, Whittaker AC, Alçiçek MC (2016). Geomorphic and geologic constraints on the active normal faulting of the Gediz (Alaşehir) Graben, Western Turkey. Journal of the Geological Society of London 173: 666-678.

Kim YS, Sanderson DJ (2005). The relationship between displacement and length of faults: a review. Earth-Science Reviews 68: 317-334.

Kong P, Fink D, Chunguang Na, Xiao W (2010). Dip-slip rate determined by cosmogenic surface dating on a Holocene scarp of the Daju fault, Yunnan, China. Tectonophysics 493: 106-112.

Lee WHK, Wu FT, Jacobsen C (1*976). A catalog of historical earthquakes* in China compiled from recent Chinese publications. Bulletin of the Seismological Society of America 66: 2003-2017.

Liu BL, Phillips FM, Fabrykamartin JT, Fowler MM, Stone WD (1994). Cosmogenic ^{36}Cl accumulation in unstable landforms, 1. Effects of the thermal neutron distribution. Water Resources Research 30 (11): 3115-3125.

Manighetti I, Caulet C, Barros L, Perrin C, Cappa F et al. (2015). Generic along-strike segmentation of Afar normal faults, East Africa: implications on fault growth and stress heterogeneity on seismogenic fault planes. Geochemistry, Geophysics, Geosystems 16 (2): 443-467.

Marrett R, Allmendinger RW (1991). Estimates of strain due to brittle faulting: sampling of fault populations. Journal of Structural Geology 13: 735-738.

McCalpin JP (editor) (2009). Paleoseismology. London, UK: Academic Press.

McKenzie D (1972). Active tectonics of the Mediterranean region. Geophysical Journal International 30: 109-185.

Mechernich S, Schneiderwind S, Mason J, Papanikolaou I, Deligiannakis G et al. (2018). The seismic history of the Pisia fault (eastern Corinth rift, Greece) from fault plane weathering features and cosmogenic ^{36}Cl dating. Journal of Geophysical Research: Solid Earth 2018: 2017JB014600RR.

Mitchell SG, Matmon A, Bierman, PR, Enzel Y, Caffee M et al. (2001). Displacement history of a limestone normal fault scarp, northern Israel, from cosmogenic ^{36}Cl. Journal of Geophysical Research 106 (B3): 4247- 4264.

Molnar P (1979). Earthquake recurrence intervals and plate tectonics. Bulletin of the Seismological Society of America 69 (1): 115-133.

Mouslopoulou V, Moraetis D, Benedetti L, Guillou V, Bellier O et al. (2014). Normal faulting in the forearc of the Hellenic subduction margin: paleoearthquake history and kinematics of the Spili Fault, Crete, Greece. Journal of Structural Geology 66: 298-308.

Öcal N (1958). Söke-Balat Zelzelesi. İstanbul, Turkey: İstanbul Kandilli Rasathanesi Sismoloji Yayınları (in Turkish).

Öcal N (1968). Türkiyenin Sismisitesi ve Zelzele Coğrafyası, 1850-1960 Yılları İçin Zelzele Kataloğu. İstanbul, Turkey: İstanbul Kandilli Rasathanesi Yayınları (in Turkish).

Oner Z, Dilek Y (2011). Supradetachment basin evolution during continental extension: the Aegean province of western Anatolia, Turkey. Geological Society of America Bulletin 123 (11-12): 2115-2141.

Özkaymak Ç, Sozbilir H, Uzel B, Akyuz HS (2011). Geological and palaeoseismological evidence for late Pleistocene–Holocene activity on the Manisa Fault Zone, western Anatolia. Turkish Journal of Earth Sciences 20 (4): 449-474.

Palumbo L, Benedetti L, Bourles D, Cinque A, Finkel R (2004). Slip history of the Magnola fault (Apennines, Central Italy) from ^{36}Cl surface exposure dating: evidence for strong earthquake over the Holocene. Earth and Planetary Science Letters 225: 163-176.

Pantosti D, D'Adezzio G, Cinti FR (1996). Paleoseismicity of the Ovindo-Pezza fault, central Apennines, Italy: a history including a large, previously unrecorded earthquake in the Middle Ages (860-1300 A.D.). Journal of Geophysical Research, 101 (B3): 5937-5959.

Pavlides S (1996). First palaeoseismological results from Greece. Annali di Geofisica 39: 545-555.

Pavlides S, Caputo R (2004). Magnitude versus faults' surface parameters: quantitative relationships from the Aegean Region. Tectonophysics 380: 159-188.

Perrin C, Manighetti I, Ampuero JP, Cappa F, Gaudemer Y (2016). Location of largest earthquake slip and fast rupture controlled by along-strike change in fault structural maturity due to fault growth. Journal of Geophysical Research 121 (5): 3666-3685.

Phillips FM, Stone WD, Fabryka-Martin JT (2001). An improved approach to calculating low-energy cosmic-ray neutron fluxes near the land/atmosphere interface. Chemical Geology 175 (3-4): 689-701.

Phillips FM, Zreda MG, Flinsch MR, Elmore D, Sharma P (1996). A reevaluation of cosmogenic Cl-36 production rates in terrestrial rocks. Geophysical Research Letters 23 (9): 949-952.

Pınar N, Lahn E (1952). Türkiye Depremleri İzahlı Kataloğu. Ankara, Turkey: Türkiye Cumhuriyeti Bayındırlık ve İskan Bakanlığı (in Turkish).

Şaroğlu F, Emre Ö, Kuşçu I (1992). Active Fault Map of Turkey (Scale 1:1,000,000). General Directorate of Mineral Research and Exploration. Ankara, Turkey: MTA.

Schimmelpfennig I, Benedetti L, Finkel R, Pik R, Blard PH et al. (2009). Sources of in-situ Cl-36 in basaltic rocks. Implications for calibration of production rates. Quaternary Geochronology 4 (6): 441-461.

Schlagenhauf A, Gaudemer Y, Benedetti L, Manighetti I, Palumbo L et al. (2010). Using in situ chlorine-36 cosmonuclide to recover past earthquake histories on limestone normal fault scarps: a reappraisal of methodology and interpretations. Geophysical Journal International 182 (1): 36-72.

Schlagenhauf A, Manighetti I, Benedetti L, Gaudemer Y, Finkel R et al. (2011). Earthquake supercycles in Central Italy, inferred from ^{36}Cl exposure dating. Earth and Planetary Science Letters 307 (3-4): 487-500.

Scholz CH (2002). *The Mechanics of Earthquakes and Faulting*. 2nd ed. Cambridge, UK: Cambridge University Press.

Şengör AMC (1979). The North Anatolian Transform Fault: its age, offset and tectonic significance. Journal of the Geological Society London 136: 269-282.

Şengör AMC, Görür N, Şarğlu F (1985). Strike-slip faulting and related basin formation in zones of tectonic escape: Turkey as a case study. In: Biddle K, Christie-Blick N (editors). Strike-Slip Deformation, Basin Formation and Sedimentation. Special Publications 37. Tulsa, OK, USA: Society of Economic Paleontologists and Mineralogists, pp. 227-264.

Şengör AMC, Yılmaz Y (1981) Tethyan evolution of Turkey: a plate tectonic approach. Tectonophysics 75: 181-241.

Seyitoğlu G, Scott B (1992). The age of the Büyük Menderes Graben (western Turkey) and its tectonic implications. Geological Magazine 129 (2): 239-242.

Seyitoğlu G, Scott BC (1991). Late Cenozoic crustal extension and basin formation in west Turkey. Geological Magazine 128: 155-166.

Seyitoğlu G, Scott BC, Rundle CC (1992). Timing of Cenozoic extensional tectonics in west Turkey. Journal of the Geological Society of London 149: 533-538.

Shaw B, Jackson J (2010). Earthquake mechanisms and active tectonics of the Hellenic subduction zone. Geophysical Journal International 181: 966-984.

Shebalin NV, Karnik V, Hadzievski D (editors) (1974). Catalogue of Earthquakes of the Balkan Region. I, UNDP-UNESCO Survey of the Seismicity of the Balkan region. Skopje, Yugoslavia: UNDP.

Soysal H, Sipahioğlu S, Kolçak D, Altınok Y (1981). Historical earthquake catalogue of Turkey and surrounding area (2100 B.C. – 1900 A.D.) Technical Report No: TBAG-341. Ankara, Turkey: TÜBİTAK,.

Sözbilir H (2005). Oligo-Miocene extension in the Lycian orogen: evidence from the Lycian molasse basin, SW Turkey. Geodinamica Acta 18: 257-284.

Sözbilir H, Özkaymak Ç, Uzel B, Sümer Ö, Eski S et al. (2016a). Palaeoseismology of the Havran-Balikesir Fault Zone: evidence for past earthquakes in the strike-slipdominated contractional deformation along the southern branches of the North Anatolian fault in northwest Turkey. Geodinamica Acta 28 (4): 254-272.

Sözbilir H, Sümer Ö, Özkaymak Ç, Uzel B, Güler T et al. (2016b). Kinematic analysis and palaeoseismology of the Edremit Fault Zone: evidence for past earthquakes in the southern branch of the North Anatolian Fault Zone, Biga Peninsula, NW Turkey. Geodinamica Acta 28 (4): 273-294.

Stone JO (2000). Air pressure and cosmogenic isotope production. Journal of Geophysical Research 105 (B10): 23753-23759.

Stone JO (2005). Terrestrial chlorine-36 production from spallation of iron. In: 10th International Conference on Accelerator Mass Spectrometry, Berkeley, CA, USA.

Stone JO, Allan GL, Fifield LK, Cresswell RG (1996). Cosmogenic chlorine-36 from calcium spallation. Geochimica Cosmochimica Acta 60: 679-692.

Stone JO, Evans JM, Fifield LK, Allan GL, Cresswell RG (1998). Cosmogenic chlorine-36 production in calcite by muons. Geochimica et Cosmochimica Acta 62 (3): 433-454.

Sümer Ö, Inci U, Sözbilir H (2012). Tectono-sedimentary evolution of an Early Pleistocene shallow marine fan-deltaic succession at the western coast of Turkey. Geodinamica Acta 25 (3-4): 112-131.

Sümer Ö, Inci U, Sözbilir H (2013). Tectonic evolution of the Söke Basin: extension-dominated transtensional basin formation in western part of the Büyük Menderes Graben, Western Anatolia, Turkey. Journal of Geodynamics 65: 148-175.

Synal HA, Bonani G, Dobeli M, Ender RM, Gartenmann P et al. (1997). Status report of the PSI/ETH AMS facility. Nuclear Instruments and Methods in Physics Research Section B 123 (1-4): 62-68.

Tan O, Taymaz T (2001). Source parametres of November 6, 1992 Doğanbey (İzmir) earthquake (Mw = 6.0) obtained from inversion of teleseismic body-wave for AD. In: Fourth International Turkish Geology Symposium: Work in Progress on the Geology of Turkey and Its Surroundings, Adana, Turkey, p. 171.

Tan O, Taymaz T (2003). Seismotectonics of Karaburun Peninsula and Kufladası Gulf: source parameters of April 2, 1996. Kuşadası Gulf and April 10, 2003 Seferihisar (İzmir) earthquakes. In: International Workshop on the North Anatolian, East Anatolian and Dead Sea Fault Systems: Recent Progress in Tectonics and Paleoseismology and Field Training Course in Paleoseismology, Ankara, Turkey, p. 147.

Taymaz T (1993). The source parameters of Çubukdağ (W. Turkey) earthquake of 1986 October 11. Geophysical Journal International 113: 260-267.

Taymaz T, Jackson J, McKenzie D (1991). Active tectonics of the North and Central Aegean Sea. Geophysical Journal International 106: 433-490.

Taymaz T, Tan O, Yolsal S (2004). Seismotectonics of western Turkey: a synthesis of source parameters and rupture histories of recent earthquakes. In: AGU Fall Meeting, Session T14, San Francisco-California, EOS Transactions.

Tesson J, Pace B, Benedetti L, Visini F, Delli Rocioli M et al. (2016). Seismic slip history of the Pizzalto fault (central Apennines, Italy) using in situ-produced 36Cl cosmic ray exposure dating and rare earth element concentrations. Journal of Geophysical Research: Solid Earth 121: 1983-2003.

Tikhomirov D (2014). An advanced model for fault scarp dating and paleoearthquake reconstruction, with a case study of the Gediz Graben formation (Turkey). PhD, University of Bern, Switzerland.

Tikhomirov D, Akçar N, Ivy-Ochs S, Alfimov V, Schlüchter C (2014). Calculation of shielding factors for production of cosmogenic nuclides in fault scarps. Quaternary Geochronology 19: 181-193.

Walsh JJ, Bailey WR, Childs C, Nicol A, Bonson CG (2003). Formation of segmented normal faults: a 3-D perspective. Journal of Structural Geology 25: 1251-1262.

Walsh JJ, Watterson J (1987). Distributions of cumulative displacement and seismic slip on a single normal fault surface. Journal of Structural Geology 9: 1039-1046.

Walsh JJ, Watterson J (1988). Analysis of the relationship between the displacements and dimensions of faults. Journal of Structural Geology 10: 239-247.

Wells DL, Coppersmith JK (1994). New empirical relationships among magnitude, rupture length, rupture width, rupture area, and surface displacement. Bulletin of the Seismological Society of America 84: 974-1002.

Yılmaz Y, Genç ŞC, Gürer F, Bozcu M, Yılmaz K et al. (2000). When did the western Anatolian grabens begin to develop? In: Bozkurt E, Winchester JA, Piper JDA (editors). Tectonics and Magmatism in Turkey and the Surrounding Area. London, UK: Special Publications of the Geological Society, pp. 353-384.

Yönlü Ö, Altunel E, Karabacak V, Akyüz S, Yalçıner Ç (2010). Offset archaeological relics in the western part of the Büyük Menderes Graben, (western Turkey) and their tectonic implications. Geological Society of America Special Publications 471: 269-279.

Zreda M, Noller J (1998). Ages of prehistoric earthquakes revealed by cosmogenic chlorine-36 in a bedrock fault scarp at Hebgen Lake. Science 282: 1097-1099.

Zreda MG, Phillips FM, Elmore D, Kubik PW, Sharma P et al. (1991). Cosmogenic chlorine-36 production rates in terrestrial rocks. Earth and Planetary Science Letters 105: 94-109.

Appendix A. Sample and carrier weight, $^{37}Cl/^{35}Cl$ ratio, and uncertainty of samples of Priene–Sazlı Fault.

Sample	Sample weight (g)	Carrier (mg)	$^{37}Cl/^{35}Cl$ (%)	Error (%)	$^{36}Cl/^{35}Cl$ (10^{-12})	Error (%)
BL-CL-12		2.00	0.16	2.1	0.006	14.3
PRI-A1	64.54	1.01	3.6	0.5	0.495	3.7
PRI-A10	63.48	1.00	7.7	0.4	0.318	3.6
PRI-A20	66.13	1.00	4.2	0.5	0.338	4.3
PRI-A30	64.47	1.00	1.8	0.6	0.318	3.8
PRI-A40	61.15	1.00	3.9	0.6	0.244	4.3
PRI-A50	61.04	1.00	4.0	0.6	0.230	4.4
PRI-A60	57.40	1.00	1.1	1.3	0.181	5.0
PRI-B1	64.15	1.00	4.4	0.8	0.187	4.9
PRI-B10	64.41	1.00	3.6	0.8	0.161	5.5
PRI-B16	62.88	1.00	2.44	1.00	0.148	5.0
PRI-C10	63.19	1.00	4.26	1.6	0.152	4.3
PRI-D1	63.03	1.00	6.39	1.2	0.148	4.4
PRI-D10	63.95	1.00	9.01	1.8	0.114	5.9
BL-CL-13		1.99	0.2	0.9	0.004	18.4
PRI-A5	63.23	1.00	2.8	0.8	0.351	4.3
PRI-A15	62.04	1.00	6.9	1.2	0.343	4.5
PRI-A25	61.36	1.00	1.7	0.7	0.278	4.4
PRI-A35	62.28	0.99	3.8	1.3	0.284	4.1
PRI-A45	62.66	1.00	3.1	1.2	0.235	4.8
PRI-A55	62.02	1.00	4.6	0.9	0.191	4.8
PRI-A65	62.78	1.00	2.5	0.8	0.168	6.1
PRI-A70	62.75	1.00	3.8	1.1	0.157	5.1
PRI-A72	62.47	0.99	5.2	1.4	0.167	5.0
PRI-A73	62.42	1.00	3.9	1.4	0.158	5.0
PRI-B5	65.72	1.00	3.8	0.9	0.193	6.2
PRI-B15	62.28	1.00	2.8	0.8	0.179	5.7
PRI-C1	61.11	1.00	4.9	1.2	0.154	5.1
PRI-C5	60.25	1.00	4.8	0.9	0.149	5.1
PRI-C15	62.65	1.00	3.4	0.9	0.165	4.9
PRI-D5	64.56	1.00	9.6	1.6	0.133	5.5
BL-CL-14		1.99	0.16	1.7	0.006	17.4
PRI-A3	62.57	1.01	4.94	1.3	0.392	2.9
PRI-A7	63.10	1.01	2.95	0.9	0.367	3.4
PRI-A12	61.13	1.01	4.05	1.5	0.318	3.5
PRI-A17	62.56	1.01	2.83	0.7	0.336	3.4
PRI-A22	61.52	1.01	4.23	1.4	0.302	3.7
PRI-A27	61.44	1.01	4.65	0.9	0.247	3.9
PRI-A32	60.83	1.01	3.89	1.6	0.274	3.7
PRI-A37	59.12	1.01	6.03	1.6	0.210	4.3
PRI-A42	59.41	1.01	2.51	1.2	0.207	4.3

Appendix A. (Continued).

PRI-A47	59.72	1.01	3.56	1.1	0.210	3.7
PRI-A52	60.77	1.00	2.54	1.1	0.184	4.0
PRI-A57	62.17	1.00	2.27	0.6	0.200	4.5
PRI-A62	63.31	1.00	2.47	0.8	0.172	4.6
PRI-A67	61.81	0.99	3.55	1.1	0.130	7.0
PRI-B7	63.27	1.00	3.31	0.3	0.194	4.9
PRI-B12	63.51	1.00	2.85	0.8	0.165	4.9
BL-CL-15		4.37	0.14	1.3	0.005	21
PRI-A6	63.73	1.00	7.41	0.7	0.351	4.5
PRI-A13	63.51	1.00	4.84	0.4	0.343	4.4
PRI-A19	62.04	1.00	2.25	0.7	0.384	4.3
PRI-A26	65.12	1.00	4.27	0.5	0.331	4.6
PRI-A33	63.45	1.00	4.92	0.5	0.288	4.1
PRI-A39	63.79	1.00	4.94	0.6	0.205	5.5
PRI-B3	64.43	1.00	3.72	1.6	0.181	5.6
PRI-B6	62.51	1.00	2.86	1.9	0.171	6.1
PRI-B9	64.86	1.00	3.18	1.2	0.179	5.7
PRI-B13	64.96	1.00	2.81	1.0	0.200	5.6
PRI-C4	62.52	1.00	4.08	1.4	0.183	5.6
PRI-C8	61.32	0.99	4.62	0.3	0.165	5.9
PRI-C12	61.51	1.00	4.43	1.4	0.177	5.8
PRI-C16	64.02	0.99	5.09	0.7	0.144	4.7
PRI-D4	64.28	0.99	12.44	1.0	0.126	6.0
PRI-D8	62.98	1.00	9.15	0.9	0.125	5.8
BL-CL-16		1.01	0.18	1.56	0.006	29.8
PRI-C02	65.77	1.01	4.81	0.82	0.171	4.6
PRI-C03	63.12	1.00	3.84	1.05	0.173	5.2
PRI-C06	65.16	1.01	5.08	0.73	0.166	4.6
PRI-C07	67.42	1.01	4.43	0.91	0.172	4.5
PRI-C09	61.05	1.01	5.44	0.67	0.134	5.1
PRI-C11	67.37	1.01	4.30	1.04	0.156	5.0
PRI-C13	64.60	1.00	4.44	0.73	0.162	4.6
PRI-C14	65.85	1.00	4.05	0.77	0.175	4.0
PRI-C17	66.65	1.00	6.32	1.01	0.165	4.6
PRI-D02	62.53	1.01	5.21	0.89	0.148	4.8
PRI-D03	66.50	1.01	11.25	0.71	0.128	4.7
PRI-D06	62.87	1.01	6.82	0.89	0.132	5.0
PRI-D07	67.49	1.01	9.85	1.06	0.122	6.1
PRI-D09	65.94	1.01	9.00	1.03	0.105	5.7
BL-CL-17		1.94	0.17	1.42	0.010	26.3
PRI-A2	65.20	1.00	5.45	0.97	0.404	4.5
PRI-A4	63.73	1.00	5.27	0.79	0.379	4.5
PRI-A8	65.76	1.00	3.86	0.65	0.339	4.0

Appendix A. (Continued).

PRI-A9	62.96	1.00	5.45	0.68	0.314	4.4
PRI-A11	68.71	1.00	6.38	0.61	0.322	4.4
PRI-A14	64.57	1.00	2.77	0.52	0.361	4.0
PRI-A16	64.68	1.00	2.82	0.67	0.363	4.5
PRI-A18	69.81	1.00	1.52	0.76	0.382	4.1
PRI-B2	69.95	0.99	4.24	0.29	0.185	5.3
PRI-B4	68.60	0.99	3.89	0.15	0.175	5.5
PRI-B8	67.97	1.00	3.21	0.35	0.199	5.0
PRI-B11	65.81	1.00	2.8	0.8	0.179	5.7
PRI-B14	62.02	1.00	2.62	0.24	0.144	5.8
PRI-C18	68.96	0.99	3.85	0.26	0.165	5.6
BL-CL-18		2.99	0.15	0.79	0.000	3095.3
PRI-A21	63.21	1.00	4.71	0.775	0.337	5.2
PRI-A23	62.53	1.01	4.30	0.409	0.293	5.3
PRI-A24	64.06	1.01	4.26	0.620	0.291	5.4
PRI-A28	64.13	1.01	5.52	0.497	0.278	4.9
PRI-A29	64.16	1.01	1.75	1.060	0.316	5.5
PRI-A31	66.13	1.01	2.28	0.480	0.325	4.2
PRI-A34	60.47	1.01	2.83	0.604	0.293	4.7
PRI-A36	57.26	1.01	6.01	0.596	0.249	5.0
PRI-A38	61.14	1.01	6.26	0.746	0.216	5.3
PRI-A41	55.28	1.00	3.38	0.380	0.215	5.4
PRI-A43	62.24	1.01	2.88	0.767	0.251	5.0
PRI-A44	59.02	1.00	3.40	0.710	0.231	5.3
PRI-A46	60.55	1.02	3.99	0.705	0.228	5.1
PRI-A48	61.50	1.01	4.39	0.747	0.214	5.5
BL-CL-19		3.93	0.14	1.04	0.004	36.5
PRI-A49	58.02	1.00	4.05	0.90	0.214	5.9
PRI-A51	57.46	1.01	2.69	0.75	0.190	6.5
PRI-A53	62.44	1.01	1.72	0.95	0.198	6.3
PRI-A54	61.05	1.01	1.83	0.57	0.233	4.4
PRI-A56	59.43	1.01	2.67	31.19	0.173	47.5
PRI-A58	60.28	1.00	1.67	0.58	0.177	4.5
PRI-A59	60.62	0.01	1.52	0.94	0.190	4.9
PRI-A61	58.95	1.00	1.49	1.01	0.184	4.8
PRI-A63	63.72	1.01	2.60	1.34	0.172	5.4
PRI-A64	63.60	1.01	4.56	0.75	0.176	4.5
PRI-A66	65.36	1.01	2.97	0.65	0.161	4.5
PRI-A68	64.40	1.00	3.09	1.12	0.152	4.3
PRI-A69	60.61	1.00	2.31	0.98	0.144	4.9
PRI-A71	62.16	1.00	5.42	0.85	0.146	4.8

Appendix B. Modeling of the paleoseismic history of the fault based on databases of strip A (5 earthquakes), A (6 earthquakes), B, BCD, and ABCD.

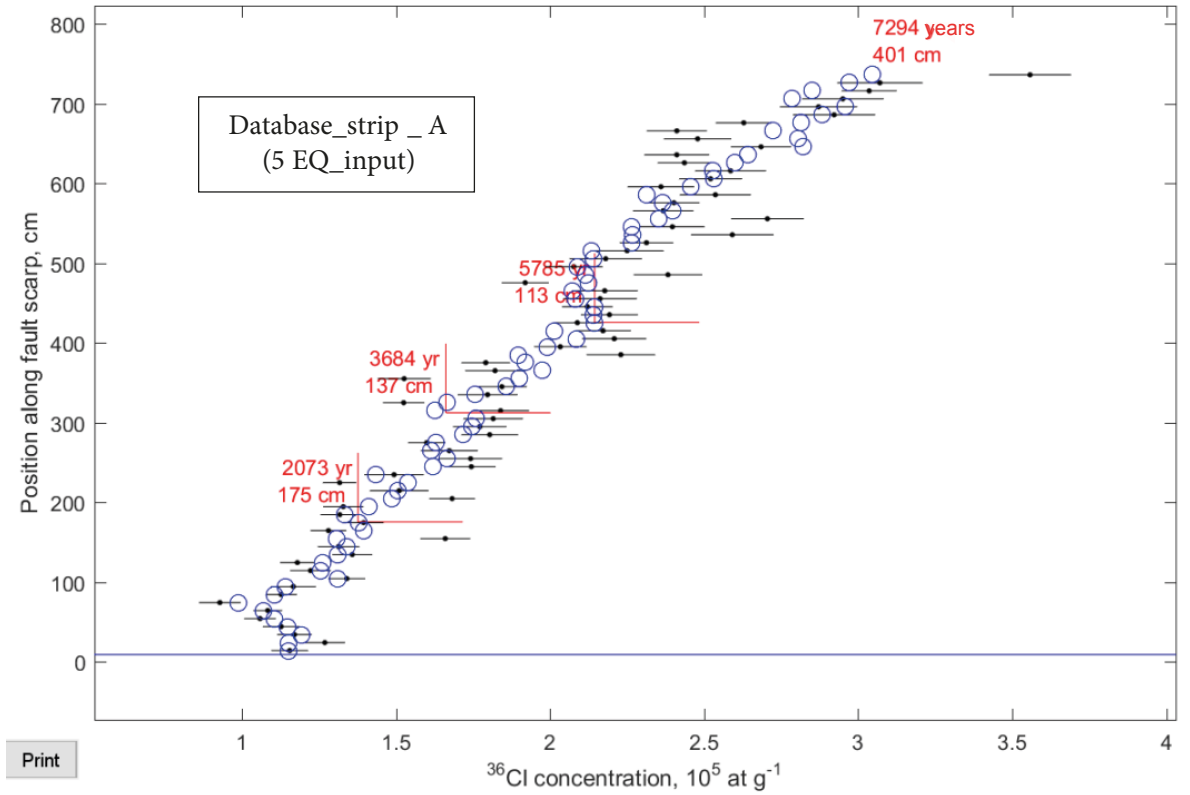

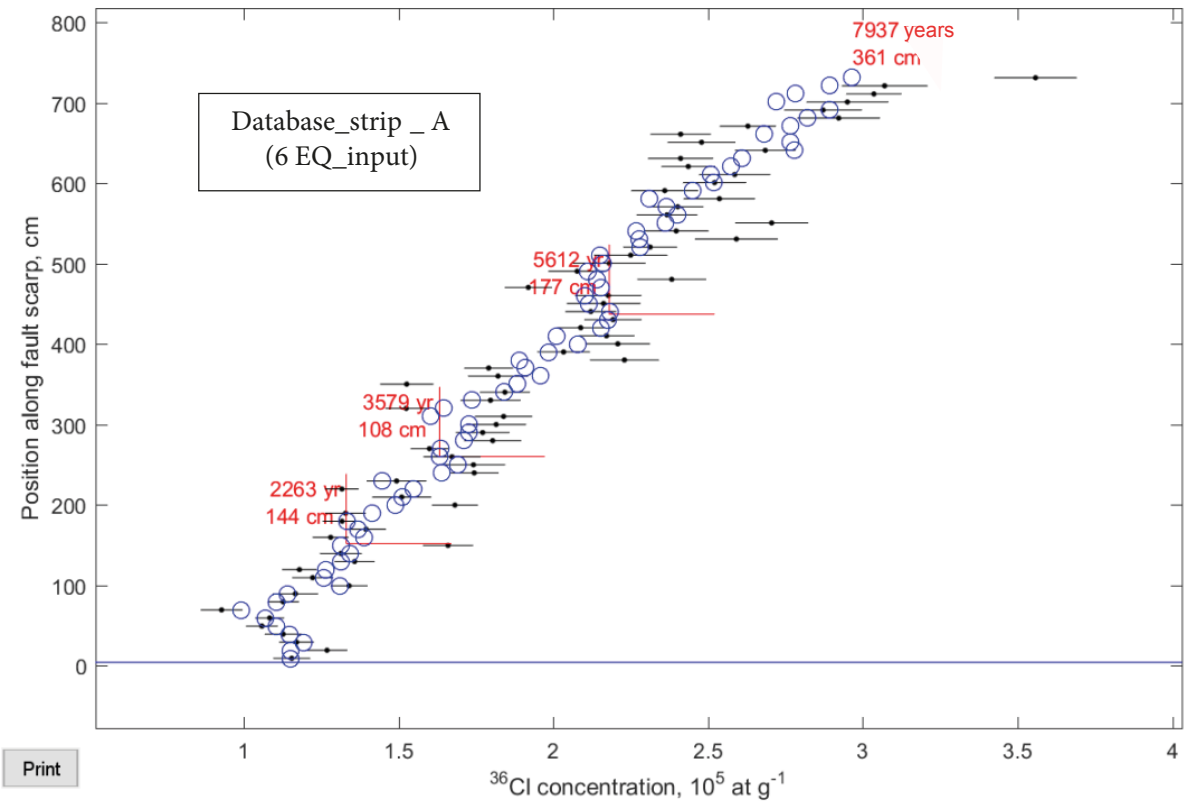

Appendix B. (Continued).

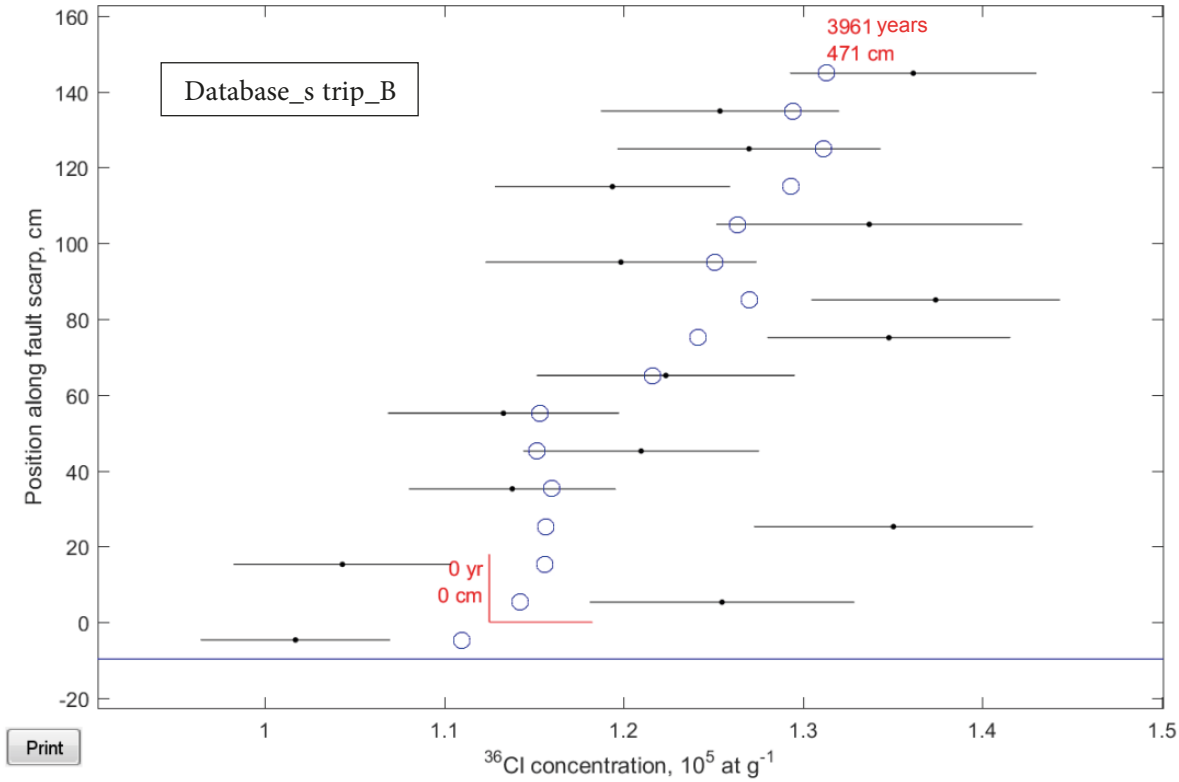

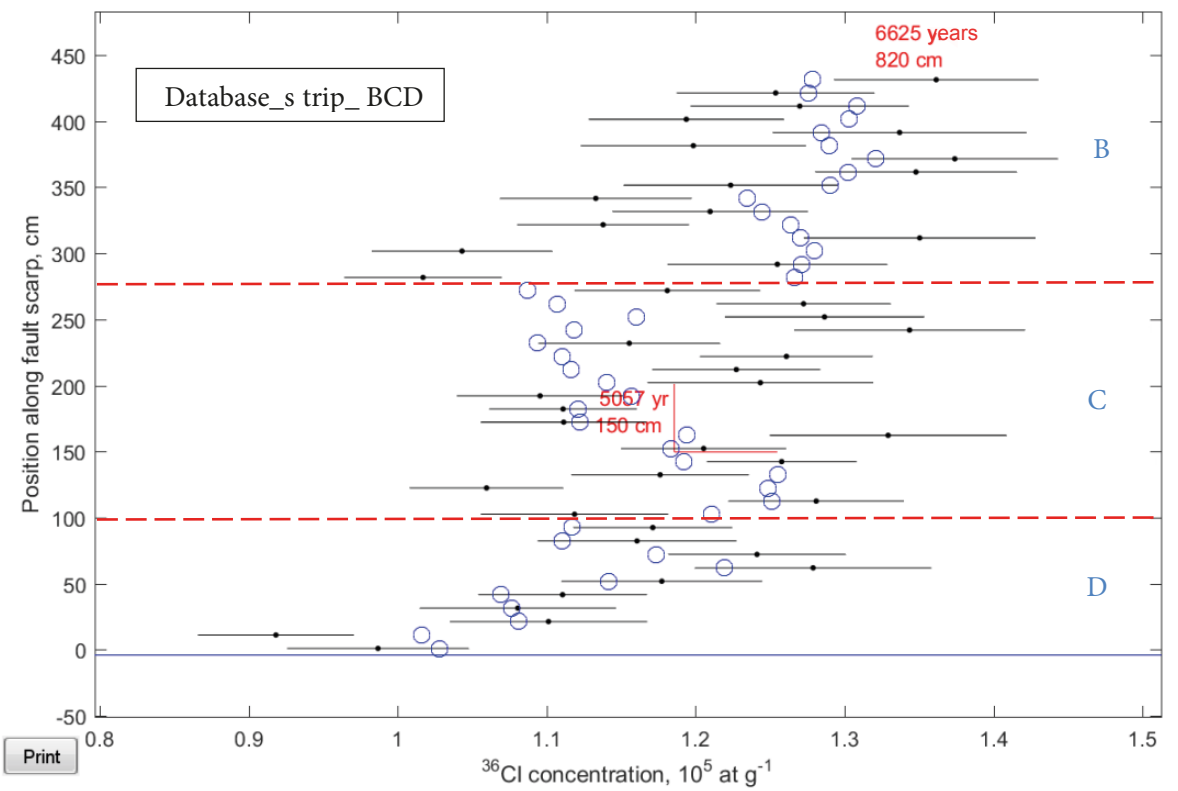

Appendix B. (Continued).

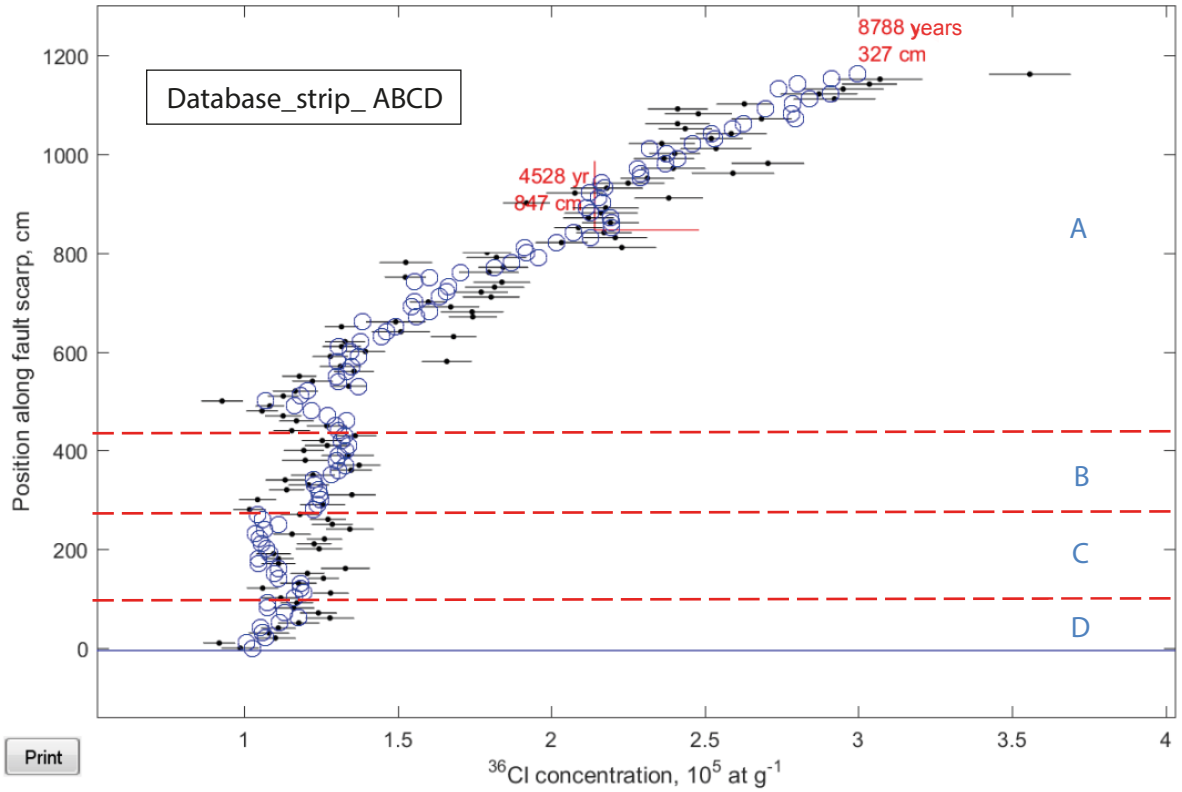

Appendix C. Fault Scarp Dating Tool – a MATLAB code for fault scarp dating with in-situ chlorine-36.

We publish a MATLAB code used to analyze the concentration profile of cosmogenic ^{36}Cl accumulated in situ through rupture history of the Priene–Sazlı fault scarp. The code is a version of the forward modeling MATLAB code, Fault Scarp Dating Tool (Tikhomirov, 2014). The code models a ^{36}Cl profile accumulated in the fault scarp surface through a guessed rupture history and compares the modeled and measured ^{36}Cl profiles with statistical tests. Rupture histories are randomly generated in bounded solution space using the Monte Carlo method or optimized using the random walk algorithm to achieve the best fit of the modeled and measured ^{36}Cl profiles. The code has a user-friendly interface, built-in help, and an example of input and output data.

Data

1. 'FSDT code' folder contains following files:

1.1 _how-to_run_the_code.txt – the text file, which explains how-to run the code.

1.2 _List of code's functions and files – the .pdf file with a list of all files of the code.

1.3 angdist.m – see CRONUS-Earth Al-26/Be-10 exposure age calculator, MATLAB function reference, Version 2: November 2007. http://hess.ess.washington.edu/math/docs/al_be_v2/al_be_fctn_desc/

1.4 antatm.m – see CRONUS-Earth Al-26/Be-10 exposure age calculator, MATLAB function reference, Version 2: November 2007. http://hess.ess.washington.edu/math/docs/al_be_v2/al_be_fctn_desc/

1.5 BalcoScaling.m – the compilation of functions make_al_be_consts_v22.m and get_al_be_age.m. See CRONUS-Earth Al-26/Be-10 exposure age calculator, MATLAB function reference, Version 2: November 2007. http://hess.ess.washington.edu/math/docs/al_be_v2/al_be_fctn_desc/

1.6 beta_ebar.m – a modification of function P_mu_total.m. See CRONUS-Earth Al-26/Be-10 exposure age calculator, MATLAB function reference, Version 2: November 2007. http://hess.ess.washington.edu/math/docs/al_be_v2/al_be_fctn_desc/

1.7 Calcnbins.m – Calculate the "ideal" number of bins to use in a histogram, using a choice of methods.

1.8 cleanXlsSheets.m – cleans an XLS-file content. http://www.mathworks.com/matlabcentral/answers/642-how-do-i-clear-the-contents-of-excel-by-sheet/

1.9 colluvium – a subfunction to calculate shielding under colluvium.

1.10 cont_mode.m – finds the modal value of a continuously distributed variable

1.11 d2r.m – see CRONUS-Earth Al-26/Be-10 exposure age calculator, MATLAB function reference, Version 2: November 2007. http://hess.ess.washington.edu/math/docs/al_be_v2/al_be_fctn_desc/

1.12 Database_Maker_Help.txt - the help file of Database Maker.

1.13 Database_Maker_Help.txt – the help file of Database Maker.

1.14 DBmaker.m – creates a database for reconstruction of the exposure history of the fault scarp.

1.15 desilets2006sp.m – see CRONUS-Earth Al-26/Be-10 exposure age calculator, MATLAB function reference, Version 2: November 2007. http://hess.ess.washington.edu/math/docs/al_be_v2/al_be_fctn_desc/

1.16 dunai2001sp.m – see CRONUS-Earth Al-26/Be-10 exposure age calculator, MATLAB function reference, Version 2: November 2007. http://hess.ess.washington.edu/math/docs/al_be_v2/al_be_fctn_desc/

1.17 fit1decay.m – approximates data with one exponential decay function.

1.18 FSDT_Database_Maker.fig – the layout description of Database Maker interface.

1.19 FSDT_Database_Maker.m – the control code of Database Maker interface.

1.20 FSDT_Simulator.fig – the layout description of Simulator interface.

1.21 FSDT_Simulator.m – the control code of Simulator interface.

1.22 fun2decay.m – returns the value of sum of two exponential decay functions.

1.23 fun3decay.m – returns value of sum of three exponential decay functions.

1.24 get_rand.m – generates a vector of random values following uniform or normal distribution.

1.25 Histogram_Overview.m – the layout description and the control code of Histogram Overview window.

1.26 lifton2006sp.m – see CRONUS-Earth Al-26/Be-10 exposure age calculator, MATLAB function reference, Version 2: November 2007. http://hess.ess.washington.edu/math/docs/al_be_v2/al_be_fctn_desc/

1.27 Main_Result.m – the layout description and the control code of Main Result window.

1.28 MonteCarloScarp.m – generates random rupture histories and collects the histories with fit chi-square value below the threshold.

1.29 muon_flux.m – a modification of function P_mu_total.m. See CRONUS-Earth Al-26/Be-10 exposure age calculator, MATLAB function reference, Version 2: November 2007. http://hess.ess.washington.edu/math/docs/al_be_v2/al_be_fctn_desc/

1.30 NCEP2.mat – see CRONUS-Earth Al-26/Be-10 exposure age calculator, MATLAB function reference, Version 2: November 2007. http://hess.ess.washington.edu/math/docs/al_be_v2/al_be_fctn_desc/

1.31 NCEPatm_2.m – see CRONUS-Earth Al-26/Be-10 exposure age calculator, MATLAB function reference, Version 2: November 2007. http://hess.ess.washington.edu/math/docs/al_be_v2/al_be_fctn_desc/

1.32 nucl_data.mat – the data file with nuclear physical constants.

1.33 Parameter_Window.m – the layout description and the control code of Resulting Parameter window.

1.34 PMag_Mar07.mat – see CRONUS-Earth Al-26/Be-10 exposure age calculator, MATLAB function reference, Version 2: November 2007. http://hess.ess.washington.edu/math/docs/al_be_v2/al_be_fctn_desc/

1.35 PointShield_mu.m – calculates the scaled flux of fast muons at the point of footwall.

1.36 PointShield_sp.m – calculates the shielding factor for high-energy neutrons at the point of footwall.

1.37 PointShield_sp_coll.m – calculates the shielding factor for high-energy neutrons at the point of colluvium surface.

1.38 PointShield_sp_th.m – calculates the apparent attenuation length in the footwall surface below colluvium.

1.39 Probability_Density_Plot.m – the layout description and the control code of Probability Density Plot window.

1.40 r2d.m – see CRONUS-Earth Al-26/Be-10 exposure age calculator, MATLAB function reference, Version 2: November 2007. http://hess.ess.washington.edu/math/docs/al_be_v2/al_be_fctn_desc/

1.41 RandomWalkScarp.m – optimizes the rupture history to achieve a minimum of the fit chi-square value.

1.42 round_from_zero.m – rounds a number to the next higher number.

1.43 Scarp_Visual_Check.m – the layout description and the control code of Visual Check window of the scarp cross-section.

1.44 ScarpSimulator.m – calculates accumulated ^{36}Cl profile according to the rupture history.

1.45 sec2hhmmss.m – converts seconds into HH.MM.SS format.

1.46 Simulator_Help.txt – the help file of Simulator.

1.47 sky – a subfunction of one formula.

1.48 spall – a subfunction of one formula.

1.49 start – the function to start FSDT with the command 'start'.

1.50 stone2000.m – see CRONUS-Earth Al-26/Be-10 exposure age calculator, MATLAB function reference, Version 2: November 2007. http://hess.ess.washington.edu/math/docs/al_be_v2/al_be_fctn_desc/

1.51 stone2000Rcsp.m – see CRONUS-Earth Al-26/Be-10 exposure age calculator, MATLAB function reference, Version 2: November 2007. http://hess.ess.washington.edu/math/docs/al_be_v2/al_be_fctn_desc/

1.52 ThermEpithermNeutronCoef.m – calculates the attenuation lengths and coefficients of two group diffusion approximation of thermal and epithermal neutrons

1.53 Topo_Visual_Check.m – the layout description and the control code of Visual Check window of the topographic shielding.

1.54 TpToTopo.m – converts the bar approximation or the broken-line approximation of the horizon line into the binary matrix of the hemisphere mesh.

1.55 Ugol.m – a subfunction of one formula.

1.56 About.txt – about text file.

2. 'Priene-Sazlı example' folder contains following folders:

2.1 'Input' folder contains following files:

2.1.1 PRIA.xlsx – the input sheet of the chemical composition and geometry of the Priene-Sazlı samples.

2.1.2 PRI_Shielding.xlsx – the input sheet of the topographical shielding of Priene-Sazlı sampling location.

2.2 'Database' folder contains following files:

2.2.1 Database A.mat' – the database of Priene-Sazlı A dataset.

2.2.2 Database A_input_data.txt – the input data of FSDT_Database_Maker used to produce the database 'Database A.mat' of Priene-Sazlı A dataset.

2.2.3 Screenshot of FSDT DBM interface.jpg – the screenshot of FSDT_Database_Maker interface with entered input data of Priene-Sazlı A dataset.